

# A unified numerical model for two-phase porous, mush and suspension flow dynamics in magmatic systems

Ying-Qi Wong<sup>1,2</sup> and Tobias Keller<sup>1,2</sup>

<sup>1</sup>*Department of Earth Sciences, ETH Zürich, 8092 Zürich, Switzerland. E-mail: [ying.wong@erdw.ethz.ch](mailto:ying.wong@erdw.ethz.ch)*

<sup>2</sup>*School of Geographical and Earth Sciences, University of Glasgow, Glasgow G12 8QQ, UK*

Accepted 2022 December 2. Received 2022 November 18; in original form 2022 April 13

## SUMMARY

Magmatic systems in the Earth's mantle and crust contain multiple phases including solid crystals, liquid melt and low viscosity fluids. Depending on depth, tectonic setting and chemical composition, magmatic systems can range from partially molten rock at low melt fraction to magma mushes at intermediate melt fraction to magmatic suspensions at high melt fraction. However, the theories underpinning most process-based models of magmatic systems describe magma as a single-phase fluid, or as a two-phase mixture either in the porous flow regime at low melt fractions or in the suspension flow regime at high melt fractions. Connections between the two-phase end-member theories are poorly established and hinder investigations into the dynamics of mush flows at intermediate phase fractions, leaving a significant gap in bridging trans-crustal magma processing from source to surface. To address this knowledge gap and unify two-phase magma flow models, we develop a 2-D system-scale numerical model of the fluid mechanics of an  $n$ -phase system at all phase proportions, based on a recent theoretical model for multiphase flows in igneous systems. We apply the model to two-phase, solid-liquid mixtures by calibrating transport coefficients to theory and experiments on mixtures with olivine-rich rock and basaltic melt using a Bayesian parameter estimation approach. We verify the model using the method of manufactured solutions and test the scalability for high resolution modelling. We then demonstrate 1-D and 2-D numerical experiments across the porous, mush and suspension flow regimes. The experiments replicate known phenomena from end-member regimes, including rank-ordered porosity wave trains in 1-D and porosity wave breakup in 2-D in the porous flow regime, as well as particle concentration waves in 1-D and mixture convection in 2-D in the suspension flow regime. By extending self-consistently into the mush regime, the numerical experiments show that the weakening solid matrix facilitates liquid localization into liquid-rich shear bands with their orientation controlled by the solid stress distribution. Although the present model can already be used to investigate three-phase mixtures using conceptually derived transport coefficients, more rigorous calibration to experiments and end-member theories is needed to ensure accurate timescales and mechanics. With a self-consistent way to examine multiphase mixtures at any phase proportion, this new model transcends theoretical limitations of existing multiphase numerical models to enable new investigations into two-phase or higher magma mush dynamics.

**Key words:** Numerical modelling; Mechanics, theory, and modelling; Magma chamber processes; Physics of magma and magma bodies.

## 1 INTRODUCTION

Magma ascent and processing in the Earth's mantle and crust involves multiple phases including solid crystals, liquid melt and, in shallow regions, volatile-rich fluids (Cashman & Giordano 2014; Caricchi & Blundy 2015; Sparks *et al.* 2019, and references therein). In the asthenosphere, melts can be generated by decompression or

the breakdown of hydrated minerals, but typically exist at low fractions (Hirth & Kohlstedt 1996; Cashman & Edmonds 2019). As melts ascend through the asthenosphere and into the lithosphere, further melting and accumulation can form regions with locally higher melt fraction (Lissenberg *et al.* 2013; Katz *et al.* 2022). Prolonged and spatially extensive accumulation can develop into magma reservoirs, which are thought to exist in a mush state (Annen *et al.* 2006;

Costa *et al.* 2010; Bachmann & Huber 2016; Cooper 2017; Holness *et al.* 2019). At active volcanoes, these magma mushes may undergo further differentiation and segregation, possibly accompanied by volatile exsolution that produces separate supercritical fluids, vapours and/or brines (Driesner & Heinrich 2007; Edmonds & Woods 2018). For eruptions to occur, enough of the melt phase has to segregate to form melt-rich, crystal-poor zones that have a low enough viscosity to be mobilized rapidly and erupt at the surface (Bachmann & Bergantz 2008; Bachmann & Huber 2019; Sparks *et al.* 2019; Lu *et al.* 2022). Therefore, from source to surface, the number of phases and range of phase fractions in magmatic systems spans partially molten rock at low melt fraction to magma mushes at intermediate melt fraction to magmatic suspensions at high melt fraction.

Due to the interplay of thermal, chemical and mechanical processes that cannot be directly observed, physical models are needed to test the trans-crustal magmatic processes implied by geological, geochemical and geophysical observations. The theory underpinning these models has previously been limited to single-phase flow or end-member porous and suspension flow regimes in two-phase, solid–liquid systems (e.g. McKenzie 1984; Huber *et al.* 2009; Huber & Parmigiani 2018; Bachmann & Huber 2019). We introduce these theories in the following paragraphs. We specifically highlight the distinction between each theory and their respective numerical implementations, which may introduce numerical stabilizations to transcend their theoretical limitations and enable important insights into magma processing at intermediate phase fractions (e.g. Dufek & Bachmann 2010; Jackson *et al.* 2018; Schmeling *et al.* 2019).

Single-phase flow models assume that magma moves as a homogeneous fluid, implying that phase segregation is negligible. These models tend to adopt the Stokes flow equations. Multiple phases can be simulated in such models by tracking the spatial and temporal variations in phase fraction and their impact on material properties (e.g. density, viscosity), but no differential motion between phases is allowed. Numerical implementations of these models have been used to study the role of phase change reactions such as crystallization or volatile exsolution in driving convection (e.g. Brandeis & Jaupart 1986; Longo *et al.* 2006), the time taken to trigger eruptions following mafic magma recharge into a silicic reservoir (Snyder 2000), as well as the efficiency of convective mixing in homogenizing magma reservoirs on the system scale (Huber *et al.* 2009).

To track phase segregation, which is the differential transport of phases relative to one another, the velocity field of each phase must be resolved. In the solid-dominated limit, most studies apply the porous flow and compaction theory of McKenzie (1984), which was developed for melt extraction from partially molten rock at low melt fractions (<10 per cent) in the mantle. In this model, the ascent of the buoyant liquid phase by pervasive porous flow is accommodated by viscous compaction of the denser and stiffer but permeable rock matrix. Compaction occurs on a characteristic length scale called the compaction length, which depends on the matrix permeability and the shear viscosities of the matrix material and pore liquid. For typical mantle properties, the compaction length is on the order of hundreds of meters to kilometres (Katz 2022, chapter 6). Porous flow and compaction can cause liquid-rich perturbations to propagate as waves through the matrix faster than the velocity of the percolating liquid (Spiegelman 1993a). Under specific material properties, these perturbations may evolve as solitary waves, which are shape-preserving waves that travel at a constant speed proportional to their amplitude (Scott & Stevenson 1984; Barcilon & Richter 1986; Stevenson & Scott 1991; Simpson & Spiegelman 2011). Having been developed for

partially molten magmatic systems where the melt viscosity is much less than that of the matrix, the compaction model neglects shear stresses in the pore liquid. This assumption breaks down when the solid fraction decreases below the disaggregation threshold (~20–40 per cent liquid fraction). Here, solid grains lose contact with one another and shear deformation of the liquid phase becomes important, thus the melt viscosity can no longer be neglected (Rudge 2018). Microstructural evidence from grain orientation and deformation in cumulates have sometimes (Philpotts & Philpotts 2005; Zieg & Marsh 2012; Bertollett *et al.* 2019) but not always (Holness *et al.* 2017) indicated viscous compaction as an important process.

Numerical implementations of the compaction model in the solid-dominated regime have confirmed the existence of solitary waves in one, two and three dimensions (Scott & Stevenson 1986; Barcilon & Lovera 1989; Wiggins & Spiegelman 1995). Further numerical models investigated the impact of matrix rheology, showing that liquid-rich instabilities or melt bands may develop if the matrix is strongly weakened by the presence of liquid, and the orientation of these localized bands can be controlled by the stress orientation in the matrix or a shear-weakening matrix rheology (Stevenson 1989; Holtzman *et al.* 2003; Katz *et al.* 2006). If the thermodynamics of phase change is included, some reactions can enhance matrix permeability and form reactive melt channels by the reactive infiltration instability (Aharonov *et al.* 1995; Kelemen *et al.* 1995; Spiegelman *et al.* 2001; Rudge *et al.* 2011; Weatherley & Katz 2012; Keller & Katz 2016; Rees Jones *et al.* 2018).

In the liquid-dominated limit, magma is modelled as a particulate suspension. Solid particles (silicate crystals) settle out of the liquid phase by Stokes settling (e.g. Sparks *et al.* 1984; Martin & Nokes 1988; Dufek & Bachmann 2010; Gutiérrez & Parada 2010). The particle settling speed is proportional to the density contrast between the phases and the square of the particle size, but is inversely proportional to the liquid viscosity. As the solid fraction increases, the settling speed decreases due to more pronounced backflow between nearby particles, potentially producing correlated particle settling (Zahn *et al.* 1997; Segrè *et al.* 2001; Mucha *et al.* 2004) and particle concentration waves (Manga 1996; Drew & Passman 1999) on length scales larger than an individual crystal. Numerical investigations at low Reynolds numbers show that particle-driven convection tends to be substantially faster than the settling speed of individual particles (Martin & Nokes 1988; Culha *et al.* 2020). Numerical models of suspension flow with hindered settling have been extended to include gas bubbles and explain the phase and compositional evolution as magma mixes in a reservoir (Ruprecht *et al.* 2008; Gutiérrez & Parada 2010). Having been developed for low solid fraction magmatic systems where solid grains do not or seldom collide, the suspension flow with particulate settling model neglects stresses in the solid phase. This assumption breaks down when the particle fraction approaches the close random packing limit. As solid grains come into contact, they transmit stresses along force chains and develop a matrix pressure distinct from the melt phase (e.g. Bergantz *et al.* 2017; Hoyos *et al.* 2022).

The above theories and their respective numerical implementations have been useful to understand the mechanics and timescales involved in magma ascent, accumulation and mixing, but are technically applicable only at specific limits of phase fractions. To investigate the mush regime at intermediate phase fractions, relevant for crustal magma bodies, a few studies have extended either the compaction model beyond the disaggregation threshold (~20–40 per cent liquid fraction) or the Stokes settling model beyond the close packing limit (~30–60 per cent liquid fraction).

Bercovici *et al.* (2001) derived phase-symmetrical equations including surface tension terms valid for general two-phase, solid–liquid systems but limited their analysis to the solid-rich regime, essentially recovering the compaction model. Numerical models extending the compaction model beyond the disaggregation threshold have explored thermal, chemical and mechanical processes enabling melt extraction and ascent from partially molten rock and magma mushes (e.g. Rabinowicz *et al.* 2001; Dufek & Bachmann 2010; Keller *et al.* 2013; Jackson *et al.* 2018; Schmeling *et al.* 2019). However, due to the assumption of negligible melt viscosity inherent to the compaction model, these approaches require regularizations at high melt fraction which do not emerge naturally from the governing physics. The numerical model of Dufek & Bachmann (2010) also extended the Stokes settling model beyond the close packing limit to explain compositional gaps in volcanic products, but again encounter the problem of regularizing the transition. As a result, it is difficult to evaluate how the regularizations impact the simulation of mush dynamics, or even their range of applicability within the phase fraction space. Furthermore, for the purpose of understanding trans-crustal magma mushes, where the magmatic volatile phase likely plays an important role, these models are not easily extendable to mixtures with a higher number of phases (first extensions of compaction and suspension models to three phases in Huber & Parmigiani 2018; Gutiérrez & Parada 2010 respectively).

To compare processes involved in the range of phase proportions from partially molten rock (low melt fraction) to magma mushes (intermediate melt fraction) to magmatic suspensions (high melt fraction), we require a general theory that describes the physics at any phase fraction. Recent theoretical studies by Keller & Suckale (2019) and Oliveira *et al.* (2018) derived conservation equations for multiphase, multicomponent reactive transport using the volume and ensemble averaging methods respectively, enabling not only a unified, self-consistent model across phase fraction, but also extensions to mixtures with more than two phases. Keller & Suckale (2019) further derived effective transport coefficients (analogous to viscosity, permeability, etc.) as emerging consistently from the pure-phase properties, phase fractions and assumptions regarding the connectivity of microscopic phase constituents in the mixture. This approach enables the transport coefficients, and consequently the model, to be theoretically defined as well as practically applicable across the phase space.

Building on the theory from Keller & Suckale (2019), we present a numerical model for the mechanical evolution (i.e. isothermal, isochemical, no phase change reactions) of  $n$ -phase systems. The model is written in MATLAB and available at the links in the Data Availability statement. The goal of this paper is to summarize the theory and describe the implementation of the unified numerical model with a focus on two-phase flow dynamics across the porous, mush and suspension flow regimes. We calibrate the transport coefficients using a Bayesian parameter estimation procedure (Section 4), and then verify the model using the Method of Manufactured Solutions with convergence testing (Section 5).

We demonstrate model capabilities with 1-D and 2-D simulations in the porous, mush and suspension flow regimes for two-phase mixtures. All simulations are conducted using the same numerical model at different initial phase fractions and by selecting the appropriate numerical resolution. 1-D column models are ideal for studying buoyancy-driven phase segregation, while 2-D setups resolve the effect of shear stresses and thus mixture flow. The models are validated against well-known phenomena in end-member flow regimes, including porosity wave trains in 1-D (Section 6.1) and porosity wave breakup in 2-D (Section 6.2) in the porous flow

regime, as well as particle concentration waves in 1-D (Section 6.3) and mixture convection in 2-D (Section 6.4) in the suspension flow regime. The model extends to the mush regime, where liquid localization becomes important (Sections 6.5 and 6.6). We finally demonstrate an example of three-phase flow with conceptually calibrated transport coefficients (Section 6.7). With a self-consistent way to examine multiphase mixtures at any phase proportion, this new model transcends the theoretical limitations of existing multiphase numerical models and advances investigations into two-phase or higher magma mush dynamics.

## 2 CONTINUUM MODEL

### 2.1 Governing equations

The model applies the mechanical equations (no thermochemical evolution, no reactions) from the framework of Keller & Suckale (2019), where a detailed derivation can be found. Here we present a condensed summary of the governing equations. The model describes a system containing  $n$  material phases, with each phase  $i = 1, \dots, n$  represented by its continuum-scale phase volume fraction  $\phi^i$ , pressure  $P^i$  and velocity  $\mathbf{v}^i$ . All variables and parameters vary in space and time, unless noted otherwise. Under the assumptions of constant pure-phase densities and high pure-phase viscosities (Reynolds number much less than unity), the mechanical evolution of the system consists of the conservation of mass and momentum for each phase  $i$ ,

$$\nabla \cdot \mathbf{q}_\phi^i + \Gamma_\phi^i = 0, \quad (1a)$$

$$\nabla \cdot \mathbf{q}_v^i + \Gamma_v^i = \phi^i \rho^i \mathbf{g}. \quad (1b)$$

Eq. (1a) expresses that, since the mass of each phase is constant, the divergence of intra-phase volume flux  $\mathbf{q}_\phi^i$  balances interphase volume transfer  $\Gamma_\phi^i$ . Eq. (1b) expresses that the intraphase momentum flux  $\mathbf{q}_v^i$  balances interphase momentum transfer  $\Gamma_v^i$  and the momentum source, that is, the gravitational body force induced by the volume fraction  $\phi^i$ , phase density  $\rho^i$  and gravitational acceleration  $\mathbf{g}$ . The system evolves with time through the interphase volume transfer  $\Gamma_\phi^i \equiv \partial \phi^i / \partial t$ . Assuming that the aggregate is saturated, any decrease in the phase fraction  $\phi^i$  within a control volume over time must be compensated by an increase in other phase fractions such that  $\sum_i \phi^i = 1$  holds. In this way, phase  $i$  ‘transfers’ the volume fraction it previously occupied to the other phases.

### 2.2 Constitutive relations: transfers and fluxes

Keller & Suckale (2019) derived constitutive relations to describe the transfers and fluxes constrained by the non-negativity of entropy production. Transfers describe the change in phase volume fraction or momentum due to imbalances among the phases, which can be understood as a measure of phase disequilibrium. The system addresses these imbalances by transferring volume or momentum from one phase to another. To describe transfers, we necessarily need to describe the imbalances. Taking differences between all possible phase pairs in an  $n$ -phase system quickly grows intractable, hence Keller & Suckale (2019) introduce a common reference state, from which deviations will drive transfers. For a property  $\mathbf{a}$  (representing pressure, velocity, etc.), the reference state is  $\mathbf{a}^* = \sum_i \omega_a^i \mathbf{a}^i$ , where  $\omega_a^i$  are weights that represent how fast phase  $i$  equilibrates towards the reference state and will be defined below. Transfers are driven by the deviation from the reference state  $\Delta \mathbf{a}^{i*} = \mathbf{a}^i - \mathbf{a}^*$ . Conceptually,

the phase that is most abundant and equilibrates the fastest will dominate the reference state. The other phases equilibrate towards this reference state, albeit at slower rates.

For the mechanical system, the constitutive relations describing volume transfer  $\Gamma_\phi^i$  and momentum transfer  $\Gamma_v^i$  are

$$\Gamma_\phi^i = C_\phi^i \Delta P^{i*} - \mathbf{v}^* \cdot \nabla \phi^i \quad (2a)$$

$$\Gamma_v^i = C_v^i \Delta \mathbf{v}^{i*} - P^* \nabla \phi^i. \quad (2b)$$

The transfer rates reveal the conjugate relationships between volume and pressure, and between momentum and velocity. Volume transfer occurs due to deviation of pressure from the reference state  $\Delta P^{i*}$  modulated by the volume transfer coefficient  $C_\phi^i$  (described in the next Section) and reduced by the advection of phase fraction with the reference velocity. Momentum transfer occurs due to the deviation of velocity from the reference state  $\Delta \mathbf{v}^{i*}$ , modulated by the momentum transfer coefficient  $C_v^i$  and reduced by the reference pressure field acting on gradients of phase fraction. This second term can be interpreted as arising from the net force generated by pressure acting on phase interfaces. The pressure and velocity deviations weighted by phase fraction give the compaction pressure  $\phi^i \Delta P^{i*}$  and segregation flux  $\phi^i \Delta \mathbf{v}^{i*}$ , respectively.

The transfer coefficients  $C_\phi^i, C_v^i$  are non-negative scalars where larger  $C_\phi^i, C_v^i$  imply faster equilibration of phase  $i$ . To ensure that transfers sum to zero across all phases, Keller & Suckale (2019) choose the reference state to be the weighted sum of phase states with weights  $\omega_a^i$  given by the transfer coefficients normalized to their sum over all phases,

$$P^* = \sum_i \omega_{C_\phi}^i P^i = \sum_i \frac{C_\phi^i}{\sum_k C_\phi^k} P^i, \quad (3a)$$

$$\mathbf{v}^* = \sum_i \omega_{C_v}^i \mathbf{v}^i = \sum_i \frac{C_v^i}{\sum_k C_v^k} \mathbf{v}^i. \quad (3b)$$

As a result, the reference state is dominated by the state of the most abundant and most rapidly equilibrating phase.

Fluxes describe the evolution of phase volume fraction and momentum due to spatial gradients within each phase. For the mechanical system, volume flux  $\mathbf{q}_\phi^i$  and momentum flux  $\mathbf{q}_v^i$  are driven by the forcing gradients of pressure and velocity, respectively,

$$\mathbf{q}_\phi^i = -K_\phi^i \Delta (\nabla P)^{i*} + \phi^i \mathbf{v}^i, \quad (4a)$$

$$\mathbf{q}_v^i = -K_v^i \mathbf{D}^i + \phi^i P^i \mathbf{I}. \quad (4b)$$

In the volume flux, the first term is the diffusive part, driven by the deviation of pressure gradient from the reference gradient  $\Delta (\nabla P)^{i*} = (\nabla P)^i - (\nabla P)^*$ , while the second term  $\phi^i \mathbf{v}^i$  is the advective part. The volume diffusion flux is modulated by the volume flux coefficient  $K_\phi^i$  (see next section). This term represents how local-scale velocity fluctuations cause diffusion of phase fractions on the system scale and is most relevant for liquid-rich systems (Keller & Suckale 2019). The momentum flux comprises a deviatoric part containing the deviatoric strain rate tensor  $\mathbf{D}^i$  and an isotropic part (containing the identity matrix  $\mathbf{I}$ ). Similar to the formulation of the transfers, the flux coefficients  $K_\phi^i, K_v^i$  are non-negative scalars. As with the transfers above, the volume diffusion flux is formulated in terms of phase deviations from a reference state to implicitly satisfy the zero sum constraint imposed by mass balance, that is that  $\sum_i \mathbf{q}_\phi^i = 0$ . The reference pressure gradient is the flux-coefficient weighted sum of phase-wise pressure gradients,

$$(\nabla P)^* = \sum_i \omega_{K_\phi}^i (\nabla P)^i = \sum_i \frac{K_\phi^i}{\sum_k K_\phi^k} (\nabla P)^i. \quad (5)$$

Substituting the flux and transfer constitutive relations into (1), we obtain the governing equations as

$$\nabla \cdot [-K_\phi^i \Delta (\nabla P)^{i*} + \phi^i \mathbf{v}^i] + [C_\phi^i \Delta P^{i*} - \mathbf{v}^* \cdot \nabla \phi^i] = 0, \quad (6a)$$

$$\nabla \cdot [-K_v^i \mathbf{D}^i + \phi^i P^i \mathbf{I}] + [C_v^i \Delta \mathbf{v}^{i*} - P^* \nabla \phi^i] = \phi^i \rho^i \mathbf{g}. \quad (6b)$$

Alongside the governing equations, we have an additional equation that relates the volume transfer to the time evolution of phase fractions,

$$\frac{\partial \phi^i}{\partial t} = C_\phi^i \Delta P^{i*} - \mathbf{v}^* \cdot \nabla \phi^i. \quad (7)$$

### 2.3 Flux and transfer coefficient closures

We require material closures to describe the flux and transfer coefficients  $K_v^i, K_\phi^i, C_v^i, C_\phi^i$ , which we refer to collectively as the ‘transport coefficients’. Considering that local-scale diffusive transport facilitates fluxes and transfers, the model uses closures that depend on phase fraction, the diffusive properties of pure-phase materials,  $k_a^i$ , and some representation of the local-scale phase topology. This framework of coefficient closures is one of the novel aspects of the model, because it relates all the effective transport coefficients to a common phenomenological description of how the phases are organized in the mixture at the local scale of microscopic phase constituents such as the grain size. The pure-phase momentum diffusion parameter  $k_v^i$  is the dynamic viscosity  $\eta^i$ , which is well constrained by experiments. The pure-phase volume diffusion parameter  $k_\phi^i$  is motivated by the hindered Stokes settling speed to be  $(d^i)^2/\eta^i$ , where  $d^i$  serves as a characteristic local length scale for diffusive transport that here corresponds to solid grain size. This implies that the diffusion of volume fraction is influenced by microscale fluctuations in settling velocity in a liquid of viscosity  $\eta^i$ . The local-scale phase topology is parametrized by permission functions  $\theta_\phi^i, \theta_v^i$  (defined in the next section) that represent the connectivity of phase  $i$  in the aggregate. Combining pure-phase diffusion parameters and permission functions, the flux and transfer coefficients are

$$K_v^i = \phi^i k_v^i \theta_v^i = \phi^i \eta^i \theta_v^i, \quad (8a)$$

$$K_\phi^i = \phi^i k_\phi^i \theta_\phi^i = \frac{\phi^i (d^i)^2 \theta_\phi^i}{\eta^i}, \quad (8b)$$

$$C_v^i = \frac{\phi^i (1-\phi^i) k_v^i \theta_v^i}{(d^i)^2} = \frac{\phi^i (1-\phi^i) \eta^i \theta_v^i}{(d^i)^2}, \quad (8c)$$

$$C_\phi^i = \frac{\phi^i (1-\phi^i) k_\phi^i \theta_\phi^i}{(d^i)^2} = \frac{\phi^i (1-\phi^i) \theta_\phi^i}{\eta^i}. \quad (8d)$$

Transfer coefficients are related to flux coefficients by a factor  $(1-\phi^i)/(d^i)^2$ , reflecting that transfers vanish in the pure-phase limits, and that transfers take place over the characteristic local length scale of the grain size.

### 2.4 Permission functions

The permission functions  $\theta_a^i$  (where  $a = v, \phi$ ) are formulated as geometric averages of pure-phase diffusivity contrasts weighted by a phenomenological measure of connectivity within and between phases. This approach yields effective properties intermediate to the upper limit given by the arithmetic mean (Voigt bound) and the lower limit given by the harmonic mean (Reuss bound) in logarithmic space (useful summary in Mavko *et al.* 2009, chapter 4). This gives



the permission functions as,

$$\theta_a^i = \prod_k (M_a^{ik})^{X_\phi^{ik}} = \prod_k \left( \frac{k_a^k}{k_a^i} \right)^{X_\phi^{ik}}, \quad (9)$$

where  $M_a^{ik}$  are the pure-phase diffusive parameter contrasts and  $X_\phi^{ik}$  are the permission weights (range 0–1),

$$X_\phi^{ik} = \left( \sum_k A^{ik} S_\phi^{ik} \right) \phi^i + \left( 1 - \sum_k A^{ik} S_\phi^{ik} \right) S_\phi^{ik}, \quad (10)$$

with  $S_\phi^{ik}$  as smooth step functions in phase space,

$$S_\phi^{ik} = \frac{\left( \frac{\phi^k}{B^{ik}} \right)^{1/C^{ik}}}{\sum_j \left( \frac{\phi^j}{B^{ij}} \right)^{1/C^{ij}}}. \quad (11)$$

For each phase  $i$ ,  $A^{ik}$ ,  $B^{ik}$ ,  $C^{ik}$  are empirical fitting parameters to describe its connectivity to phase  $k$  using a smooth step function between pure-phase limits:  $0 \leq A^{ik} \leq 1$  controls the slope at the pure-phase limits,  $0 \leq B^{ik} \leq 1$  with  $\sum_k B^{ik} = 1$  controls the critical phase fraction of the step change which can be thought of as the solid disaggregation or liquid percolation threshold, and  $C^{ik} \geq 0$  controls the step width (Figs A3a and b). Ideally, these fitting parameters require calibration using existing experimental data or end-member theories for multiphase mixtures to encapsulate information on phase size, shape, compositions, surface energies and wetting behaviour. Keller & Suckale (2019) demonstrated a calibration procedure for the two-phase, solid-liquid mixture; in Section 4, we show an improved approach using the Cascading Adaptive Transitional Metropolis In Parallel (CATMIP), a Bayesian parameter estimation procedure (Minson *et al.* 2013). Since CATMIP returns posterior probability distributions, we can examine how well the experimental data or end-member theories constrain the fitting parameters while also appraising their trade-offs. Furthermore, by naturally incorporating *a priori* constraints, CATMIP will enable future calibrations for mixtures with a larger number of phases, where the limited experimental data and theoretical models will need to be complemented by conceptual assumptions to ensure well-determined calibrations.

## 2.5 Segregation-compaction length

Scaling analysis of the governing equations reveals an inherent length scale for phase segregation and compaction, called the segregation-compaction length (appendix C of Keller & Suckale 2019). This length scale is a generalization of the compaction length from McKenzie (1984) beyond the solid-dominated end-member of two-phase mixtures, and can be applied to mixtures with a larger number of phases. For a pair of phases within a multiphase mixture where phase  $j$  is segregating and phase  $k$  is compacting, the segregation-compaction length is

$$\delta_0^{jk} = \sqrt{\frac{(\phi_0^j)^2}{C_{v,0}^j} \frac{(\phi_0^k)^2}{C_{\phi,0}^k}}. \quad (12)$$

Subscripts 0 denote characteristic scales, where  $C_{v,0}^j$  and  $C_{\phi,0}^k$  are the momentum and volume transfer coefficients calculated at the characteristic phase fractions  $\phi_0^j$ ,  $\phi_0^k$ , respectively. In an  $n$ -phase mixture,  $n(n-1)$  segregation-compaction lengths exist. However, not all segregation-compaction lengths may be important, because the ratio of  $\delta_0^{jk}$  to the characteristic system scale  $\mathcal{L}_0$  (i.e. domain size, perturbation size, etc.) controls emergent dynamics (Keller

& Suckale 2019; Dohmen & Schmeling 2021). In real magmatic systems,  $\mathcal{L}_0$  could represent the magma reservoir dimension, dike width, etc. Given an  $\mathcal{L}_0$ ,  $\delta_0^{jk}$  up to one magnitude smaller implies that phase segregation will be important. In contrast, a much smaller  $\delta_0^{jk}$  implies that phases  $j$ ,  $k$  will move collectively as a mixture and the system reduces to single-phase flow. In addition to providing physical intuition, comparing  $\delta_0^{jk}$  to the system length scale informs the numerical implementation below.

## 3 NUMERICAL IMPLEMENTATION

The numerical model solves the governing eqs (6)–(7). In two dimensions, the governing equations comprise one mass balance eq. (6a), two momentum balance equations in the two spatial directions (6b), and an additional equation for the time evolution of phase fractions  $\partial\phi^i/\partial t$  for each phase  $i = 1, 2, \dots, n$  (7). These  $4 \times n$  equations are solved on a 2-D rectangular domain of size  $L_x \times L_z$  for the solution variables of horizontal velocity  $u^i$ , vertical velocity  $w^i$ , dynamic pressure  $p^i$  (reduced by lithostatic pressure) and phase fraction  $\phi^i$  fields for each phase  $i$  in space  $(x, z)$  and time  $t$ , summarized in the solution vector  $y^i(x, z, t) = [u^i, w^i, p^i, \phi^i](x, z, t)$ . The origin of the coordinate system is in the centre of the domain such that  $x \in [-L_x/2, L_x/2]$ ,  $z \in [-L_z/2, L_z/2]$ . The  $z$ -coordinate points upward.

### 3.1 Numerical discretization

The governing equations are discretized using finite differences on a staggered grid of  $N_x \times N_z$  square and equidimensional cells of size  $h$ . The domain size  $L_x \times L_z$  and the number of cells in the vertical direction  $N_z$  are taken as inputs, from which  $h$  and  $N_x$  are derived. Scalar degrees of freedom  $p^i$ ,  $\phi^i$  are located at cell centres, whereas vector velocity components  $u^i$ ,  $w^i$  are located on vertical and horizontal cell faces, respectively (e.g. Gerya 2019). Boundary conditions are applied using a row of ghost nodes along domain boundaries.

All flux and transfer coefficients are calculated on the cell centres, where  $\phi^i$  are located. Other  $p^i$ ,  $\phi^i$  or coefficients required at cell faces or corners are evaluated by arithmetic averaging from adjacent cell centres. Central differencing is used to calculate the momentum flux and its divergence. Normal ( $xx$ –,  $zz$ –) components of the deviatoric strain rate tensor are located on cell centres, while its shear ( $xz$ –) components are located on cell corners. Central differencing is also used to calculate the volume flux and its divergence. Therefore, like velocity components, horizontal volume flux components come to be located on vertical cell faces, and vertical volume flux components on horizontal faces, whereas the corresponding flux divergence terms come to be located at cell centres. The advection of phase fraction with the reference velocity in the volume transfer ( $\mathbf{v}^* \cdot \nabla\phi^i$ ) is calculated using the fifth order Weighted Essentially Non-Oscillatory scheme (WENO; Jiang & Shu 1996; detail in Appendix A).

As an alternative to the standard 2-D mode, the model can also be run in a pseudo-1-D mode. This mode is automatically selected if the specified initial condition on phase fraction does not contain horizontal variations. The 2-D-equations are solved on a grid of  $N_z$  points in the vertical direction, and one point in the horizontal direction. The horizontal momentum balance equation is still solved but horizontal velocity and flux components remain zero (within computational accuracy). This mode is applied for the 1-D column models in this study (Sections 6.1, 6.3 and 6.5). If the specified

initial condition includes variations in the horizontal direction, the equations are solved on the full 2-D,  $N_x \times N_z$  grid.

Appropriate choices of cell and domain sizes are necessary for the numerical model to converge successfully. We use the segregation-compaction length  $\delta_0^{jk}$  to guide these choices. To accomplish the goal of investigating flow regimes where both phase segregation and collective flow influence dynamics,  $\delta_0^{jk}$  must be well resolved on the grid while being 1–2 orders smaller than  $L_x, L_z$ . Tests show that at least one cell is needed to resolve each segregation-compaction length in the suspension flow regime, and at least five cells for the porous and mush flow regime (Section 5.2). On the other hand, the domain size must be at least  $10\delta_0^{jk}$  to enable (de-)compaction boundary layers to develop, as noted in compaction models which show that compaction pressures decay and segregation speeds grow exponentially away from closed boundaries or perturbations to phase fraction with the segregation-compaction length as the e-fold length (e.g. Katz 2022, chapter 6). Even larger domain sizes are needed  $\sim 40\delta_0^{jk}$  for collective flow to become appreciable.

The numerical model first evaluates pairwise  $\delta_0^{jk}$  at the selected background phase proportions and material properties. The model then takes an input for the multiple of the largest  $\delta_0^{jk}$  of the system to set the domain size. In the case of the two-phase, solid–liquid simulations shown here, the largest  $\delta_0^{jk}$  is  $\delta_0^{ls}$  (see below Section 4). The model then divides the domain size by the input number of gridpoints to determine cell size. Insufficient numerical resolution of  $\delta_0^{jk}$  will adversely affect the quality of the solution as well as solver convergence. In the mush regime, the contracting  $\delta_0^{ls}$  due to localized increases in melt fraction over time may also adversely affect solution quality. In these cases, specifying a large number of gridpoints and applying the numerical stabilizations described in Section 3.4 can improve solver robustness (more detail in the experiment shown in Section 6.5).

The time derivative enters the problem in the phase fraction eq. (7) and is discretized by the second-order, semi-implicit Crank–Nicolson scheme using central finite differencing in time. For stable numerical integration in time, the time step size is limited by either the Courant–Friedrich–Lewy (CFL) criterion on the volume flux, or by limiting volume transfer to a 1 vol per cent change in phase fraction,

$$\Delta t \leq \frac{\text{CFL}}{(\max |\mathbf{q}_\phi^i|)/(h/2) + (\max |\Gamma_\phi^i|)/0.01}, \quad (13)$$

using a specified fraction  $0 < \text{CFL} < 1$ .

### 3.2 Non-linear iterative solver

The governing equations are non-linear because constitutive relations comprise non-linear combinations of solution variables while coefficient closures are non-linear functions of phase fractions. To solve the governing equations at each time step, we apply Polyak’s heavy ball method (Polyak 1964), a pseudo-transient iterative strategy that has been applied to large numerical problems in geoscience including the two-phase compaction model due to its efficient scaling properties (e.g. Räss *et al.* 2019; Wang *et al.* 2021). Iterative methods of this kind scale better with increasing numerical resolution than direct matrix solvers. For an  $n$ -phase model with  $N_x \times N_z$  grid cells, iterative methods using  $N_{\text{it}}$  iterations only require

$\mathcal{O}(n \times N_x \times N_z \times N_{\text{it}})$  operations, while direct methods grow as  $\mathcal{O}((n \times N_x \times N_z)^3)$  operations, which tends to be much larger. Although not attempted here, pseudo-transient iterative methods require mostly local numerical operations and hence are amenable to efficient parallelization (e.g. Räss *et al.* 2019).

In the pseudo-transient method, the governing equations are put into a form of a pseudo-time-dependent equation, where the rate of change of the solution variable is the residual of the original equation. This pseudo-time-dependent equation is then integrated with explicit pseudo-time stepping until a steady-state is reached, where the rate of change (i.e. the residual) approaches zero and hence the solution to the governing equations is found. Applying this method to our model, the solution variables at the  $k$ th iteration,  $y_k^i$ , are updated using the residual at the current iteration,  $R_k^i$  and the solution guess from the previous iteration,  $y_{k-1}^i$ ,

$$y_{k+1}^i = y_k^i - \alpha \Delta \tau R_k^i + \beta (y_k^i - y_{k-1}^i), \quad (14)$$

where  $0 < \alpha < 1$  is the iterative step size control, and  $0 < \beta < 1$  acts as a damping parameter. The application of the previous iterative step scaled down by  $\beta$  has the double effect of accelerating convergence if consecutive updates point in the same direction and reducing oscillations if they do not. Damping further reduces the order of operations below power one, such that doubling the grid resolution requires fewer than double the number of iterations (Section 5.2). Larger  $\alpha, \beta$  can increase the speed of convergence, however smaller values (in particular for  $\beta$ ) result in more robust convergence.  $\Delta \tau$  is the stable pseudo-time step size. In a purely linear system of equations  $Ay = b$ ,  $\Delta \tau$  is equal to the inverse of the diagonal entries of  $A$ . In our non-linear system of governing equations, a combination of flux and transfer coefficients approximate the diagonal entries of  $A$  to derive  $\Delta \tau$ ,

$$\Delta \tau_v < \min_i \left[ \frac{K_v^i}{(h/2)^2} + (1 - \omega_{C_v}^i) C_v^i \right]^{-1}, \quad (15a)$$

$$\Delta \tau_p < \min_i \left[ \frac{K_\phi^i}{(h/2)^2} + (1 - \omega_{C_\phi}^i) C_\phi^i \right]^{-1}, \quad (15b)$$

$$\Delta \tau_\phi = \min_i \frac{1}{10} \Delta t, \quad (15c)$$

where  $\Delta \tau_v$  applies to the two velocity components,  $\Delta \tau_p$  applies to pressure and  $\Delta \tau_\phi$  applies to phase fraction.  $\omega_{C_v}^i$  and  $\omega_{C_\phi}^i$  are the weights used in averaging phase-wise fields to obtain reference velocity and pressure, respectively. Since the phase fraction equation simply relates  $\partial \phi^i / \partial t$  to  $\Gamma_\phi^i$ , we choose for  $\Delta \tau_\phi^i$  an arbitrary fraction  $< 1/10$  of the stable (physical) time step  $\Delta t$ . Testing different fractions did not affect solution convergence, because the velocity–pressure solution mainly controls convergence.

The convergence is stopped when the L2 norm of  $R_k^i$  normalized by the norm of the solution vector decreases below a specified absolute or relative convergence tolerance. The algorithm also allows for a convergence criterion by maximum number of iterations, but this should be used with caution for purposes of efficient testing only. To reduce computational time, we only update the flux and transfer coefficients and the advection term after a set number of iterations because phase fractions do not vary greatly between iterations, but the updating of coefficients requires a number of power operations which are relatively computationally expensive and would otherwise become the rate-limiting operation.

### 3.3 Boundary and initial conditions

The numerical model implementation provides a choice between closed and periodic boundary conditions. For closed boundary conditions, phase velocities and volume fluxes normal to each boundary, as well as shear stresses parallel to each boundary, are set to zero,

$$\mathbf{v}^i \left( x = \pm \frac{L_x}{2}, z, t \right) \cdot \mathbf{n} = 0, \quad (16a)$$

$$\mathbf{v}^i \left( x, z = \pm \frac{L_z}{2}, t \right) \cdot \mathbf{n} = 0, \quad (16b)$$

$$\mathbf{q}_\phi^i \left( x = \pm \frac{L_x}{2}, z, t \right) \cdot \mathbf{n} = 0, \quad (16c)$$

$$\mathbf{q}_\phi^i \left( x, z = \pm \frac{L_z}{2}, t \right) \cdot \mathbf{n} = 0, \quad (16d)$$

$$q_{v,xz}^i \left( x = \pm \frac{L_x}{2}, z, t \right) = 0, \quad (16e)$$

$$q_{v,xz}^i \left( x, z = \pm \frac{L_z}{2}, t \right) = 0, \quad (16f)$$

with  $\mathbf{n}$  the unit vector normal to the boundary. This choice of boundary conditions simulates a magmatic domain with impermeable, shear stress-free boundaries. Buoyancy-driven phase segregation is obstructed by horizontal boundaries and leads to boundary layers forming along the top and bottom of the domain.

For periodic boundary conditions, all solution variables on boundaries are set such that the solution periodically repeats itself in the horizontal and vertical directions,

$$y^i \left( x = -\frac{L_x}{2}, z, t \right) = y^i \left( x = \frac{L_x}{2}, z, t \right), \quad (17a)$$

$$y^i \left( x, z = -\frac{L_z}{2}, t \right) = y^i \left( x, z = \frac{L_z}{2}, t \right). \quad (17b)$$

These boundary conditions are used to simulate flow in a part of a larger magma reservoir, avoiding obstruction of flow and the build-up of (de-)compaction layers along boundaries. To avoid spurious solution drift due to accumulated numerical errors, we subtract the mean of the solution update after each solve.

As we assume non-inertial flow with incompressible phase materials, phase fractions are the only time-dependent solution variable for which initial conditions are required. Beyond specifying the background phase fraction, the model accepts as standard inputs the amplitude of smooth random perturbations and/or of a 2-D Gaussian perturbation at the centre of the domain. Other forms of phase fraction initial conditions can be applied by specifying a function in  $(x, z)$  in the run script.

### 3.4 Numerical stabilization

The large contrast in pure-phase solid and liquid viscosities typical for magmatic systems (here 16 orders of magnitude) can cause flux and transfer coefficients to take on vastly different magnitudes with modest changes in phase proportions. Such large coefficient contrasts can lead to numerical round-off errors and poor iterative convergence.

To stabilize the iterative scheme, we introduce two limiting controls: one to limit contrasts in permission functions within each phase across the domain, `thtlim`, and a second to limit contrasts of flux/transfer coefficients between phases `cfflim`. The first limiter `thtlim` controls the variation in permission functions within each

phase. After calculating these permission functions, the code calculates a characteristic scale for each phase by taking its geometric mean over the domain, then adjusts the permission functions by

$$\theta_{v,st}^i = \left[ \frac{1}{\theta_v^i} + \frac{\langle \theta_v^i \rangle}{\text{thtlim}^{1/2}} \right]^{-1} + \frac{\langle \theta_v^i \rangle}{\text{thtlim}^{1/2}}, \quad (18a)$$

$$\theta_{\phi,st}^i = \left[ \frac{1}{\theta_\phi^i} + \frac{\langle \theta_\phi^i \rangle}{\text{thtlim}^{1/2}} \right]^{-1} + \frac{\langle \theta_\phi^i \rangle}{\text{thtlim}^{1/2}}, \quad (18b)$$

where  $\theta_v^i, \theta_\phi^i$  are the original, unstabilized permission functions,  $\langle \theta_v^i \rangle, \langle \theta_\phi^i \rangle$  are the characteristic scales from geometric averaging over the domain, and  $\theta_{v,st}^i, \theta_{\phi,st}^i$  are the numerically stabilized permission functions. If `thtlim` is set to be much larger than the average permissions across the domain, then the limiter will have no effect and the stabilized values will be identical to the original permission functions.

The stabilized permission functions are then used to calculate the flux and transfer coefficients, on which the second limiter `cfflim` applies. The code first calculates a characteristic scale for the coefficients, again using the geometric mean. To control the coefficient contrast between phases, the code updates the coefficients using this characteristic scale and `cfflim`,

$$K_{v,st}^i = K_v^i + \frac{\max_j \langle K_v^j \rangle}{\text{cfflim}}, \quad (19a)$$

$$K_{\phi,st}^i = K_\phi^i + \frac{\max_j \langle K_\phi^j \rangle}{\text{cfflim}}, \quad (19b)$$

$$C_{v,st}^i = \left[ \frac{1}{C_v^i} + \frac{\text{cfflim}}{\min_j \langle C_v^j \rangle} \right]^{-1}, \quad (19c)$$

$$C_{\phi,st}^i = \left[ \frac{1}{C_\phi^i} + \frac{\text{cfflim}}{\min_j \langle C_\phi^j \rangle} \right]^{-1}. \quad (19d)$$

A similar notation to the permission functions applies, where the subscript `st` denotes the numerically stabilized coefficient. Among the phases, the maximum flux coefficient scale is chosen and normalized by `cfflim`, then added to all the flux coefficients. This raises smaller flux coefficients to be within `cfflim` of the maximum while leaving maximum coefficient unchanged, effectively increasing the rate of the slowest diffusive process in the system to be within `cfflim` of the fastest process. The reciprocal approach using the minimum is applied to the transfer coefficients to maintain the largest segregation velocities and compaction pressures, which are proportional to  $\Delta \mathbf{v}^{i*}, \Delta P^{i*}$  and thus inversely proportional to the transfer coefficients (2). As a result, the smallest  $\Delta \mathbf{v}^{i*}, \Delta P^{i*}$  are brought to within `cfflim` of the largest  $\Delta \mathbf{v}^{i*}, \Delta P^{i*}$ . As with the first limiter, selecting a large value for `cfflim` will nullify its effect.

## 4 CALIBRATION OF PERMISSION FUNCTIONS

We calibrate the fitting parameters  $A, B, C$  of the permission weights to represent a two-phase mixture of olivine crystals and basalt liquid due to the availability of experimental and end-member theories for that system. Each fitting parameter contains  $n \times n = 4$  elements, giving a total of 12 parameters to be determined. Keller & Suckale (2019) performed the calibration using an *ad hoc* optimization procedure, and notably showed that one set of permission weights can reasonably match the constraints on all the flux and transfer coefficients. This result reflects the common physical basis of connectivity that controls the flux and transfer of mass and momentum. Here, we improve on the calibration approach by using the

Cascading Adaptive Transitional Metropolis in Parallel (CATMIP), a Bayesian inversion algorithm (Minson *et al.* 2013; Appendix B).

To calibrate the permission weights, we apply the same experimental and theoretical constraints as in Keller & Suckale (2019). We constrain the mixture viscosity  $\sum_i K_v^i$  against the Costa *et al.* (2009) model with their parameters adjusted to match the pure-phase viscosities and slopes given by Hirth & Kohlstedt (2003) at the solid-rich end and Roscoe (1952) at the liquid-rich end. For the volume flux coefficient  $K_\phi^i$  at the solid-rich end, we are not aware of analogous models and the previous calibration suggested small  $K_\phi^i$  so that it does not contribute significantly to dynamics. The volume flux coefficient is likely most relevant for liquid-rich mixtures. We constrain  $K_\phi^s$  by sedimentation experiments quantifying the velocity correlation among solid grains (Segrè *et al.* 2001), which resemble hindered-Stokes settling using the Richardson–Zaki expression with an exponent of 5 (Richardson & Zaki 1954).

Rearranging the governing equations shows that the combination  $\phi^{\ell^2}/C_v^\ell$  corresponds to the Darcy percolation coefficient in the compaction equations (ratio of matrix permeability to liquid viscosity), thus, at the solid-rich end, we constrain  $C_v^\ell$  using the Kozeny–Carman permeability relationship. At the liquid-rich end, we constrain  $C_v^s$  using the hindered-Stokes settling coefficient. The combination  $\phi^{s^2}/C_\phi^s$  is analogous to the compaction viscosity (McKenzie 1984), for which experimental constraints are sparse (Katz *et al.* 2022). Therefore, we do not apply an independent constraint on the compaction viscosity and rather apply the compaction viscosity as  $K_v^s/\phi^\ell$ , as motivated by McKenzie (1984) and Simpson *et al.* (2010). This form of the compaction viscosity highlights that the resistance to compaction decreases with increasing melt fraction but increases to a singularity when the phase is exhausted such that divergence-free flow is obtained in incompressible single-phase systems.

Fig. 1 shows the newly calibrated permission functions using CATMIP against the experimental data and theories used as constraints. Also plotted in dotted lines is the previous calibration from Keller & Suckale (2019). Since the constraints applied are the same in both calibrations, the output permission weights and effective transport coefficients are almost identical despite differences in the calibrated values (Table 1). This result indicates that the fitting parameters are non-unique, which we can examine from their spread and correlations with other parameters using the posterior probability distributions returned by the inversion procedure (see Appendix B).

As before, we find that one set of permission functions can reasonably fit the inversion constraints, which primarily apply to the slopes of the transport coefficients towards the end-member phase fractions (Figs 1c–f). The step transition in the solid transport coefficients is mainly controlled by the adjusted Costa model. Despite similarities in the transport coefficients between the two calibrations, the velocity and pressure weights, which are calculated using arithmetic averages, differ slightly at liquid fractions above 0.4 due to small differences in the coefficient values in linear space (Figs 1g and h). These weights now approach 0.5 as the liquid fraction goes to 1, and only equal 0.5 when the liquid fraction is 1. We do not expect this minor difference to impact simulation results because solids are typically carried with the liquid suspension in this region of the phase space, implying equilibrated velocity and pressures between both phases.

With the newly calibrated  $A, B, C$ , we recalculate the segregation-compaction lengths (Fig. 2). For a two-phase system, there are two possible segregation-compaction lengths,  $\delta_0^{\ell s}$  (black lines) and  $\delta_0^{\ell \ell}$

(grey lines), however the latter remains smaller than the former and much smaller than a typical magmatic system size. Therefore, we consider  $\delta_0^{\ell s}$ , which describes liquid segregation and solid compaction, as the dominant length scale that controls flow dynamics.

Naturally, since the permission functions are very similar to those presented in Keller & Suckale (2019), the updated  $\delta_0^{\ell s}$  is also close, and we follow their definition of emergent flow regimes according to  $\delta_0^{\ell s}$ . At low liquid fractions ( $\phi^\ell < 0.08$ ),  $\delta_0^{\ell s}$  increases sharply with liquid fraction from  $< 1$  m around the percolation threshold until it reaches a maximum of 3.4 km at  $\phi^\ell \approx 0.08$ . We refer to this as the *porous flow regime*. This increasing trend is consistent with the compaction model (McKenzie 1984), where increasing liquid fraction enhances permeability, and allows more rapid liquid percolation. At intermediate liquid fractions ( $\phi^\ell = 0.08 - 0.42$ ),  $\delta_0^{\ell s}$  contracts first gradually and then more steeply with liquid fraction. We refer to this as the *mush flow regime*. With increasing liquid fraction, solid grain boundaries gradually become wetted by melt leading to the disaggregation of the contiguous solid matrix around the disaggregation threshold of  $\phi^\ell \approx 0.3$ . Contraction of the inherent length scale suggests that liquid localization will be a prominent feature in this regime. Increasing the liquid fraction further still ( $\phi^\ell > 0.42$ ) causes  $\delta_0^{\ell s}$  to decrease to the solid grain size, where it remains approximately constant for the remaining phase space. We designate this the *suspension flow regime*. We define the regime transition from mush to suspension flow where  $\delta_0^{\ell s}$  is ten times the grain size. Solids, which are no longer in contact with one another, can only sustain pressures distinct from the suspending liquid to a maximum length scale of one grain size. Therefore, phase pressure differences on the magmatic system scale will be negligible, and the dynamics reduce to the suspension model with hindered Stokes settling.

## 5 MODEL PERFORMANCE

### 5.1 Verification by the method of manufactured solutions

To verify the numerical model, we employ the method of manufactured solutions (e.g. Salari & Knupp 2000). This verification procedure substitutes an analytical expression (the ‘manufactured solution’) for the solution variables  $y^j(x, z, t) = [u^j, w^j, p^j, \phi^j](x, z, t)$  into the governing equations. Since the manufactured solution is not the exact solution to the governing equations, there will be a residual term, which can also be evaluated analytically. This residual term is encoded in the numerical model as an additional source term in the governing equations. The numerical solution forced by the analytical residual term is then compared to the analytical manufactured solution. If the numerical algorithm is implemented correctly, the numerical error should converge systematically with increasing numerical resolution.

The chosen manufactured solution should be continuous, differentiable to the order required by the problem and consistent with the boundary conditions. Furthermore, it should be similar in magnitude and spatial pattern to an expected solution to the governing equations, so that the residual term does not dominate the numerical solution. For the system of equations in this study, we choose sinusoidal solution fields with periodic boundary conditions on a square domain of side  $40\delta_0^{\ell s}$  (Fig. 3a). This domain size is large enough for both phase segregation and mixture flow to be appreciable, while still small enough to test a sufficient range of grid sizes. We show results from the suspension ( $\phi^\ell = 0.90$ ) flow regime, where we set the amplitude of the sinusoidal variations to be  $\sim [10^{-5} \text{ m s}^{-1}, 10^{-5}$



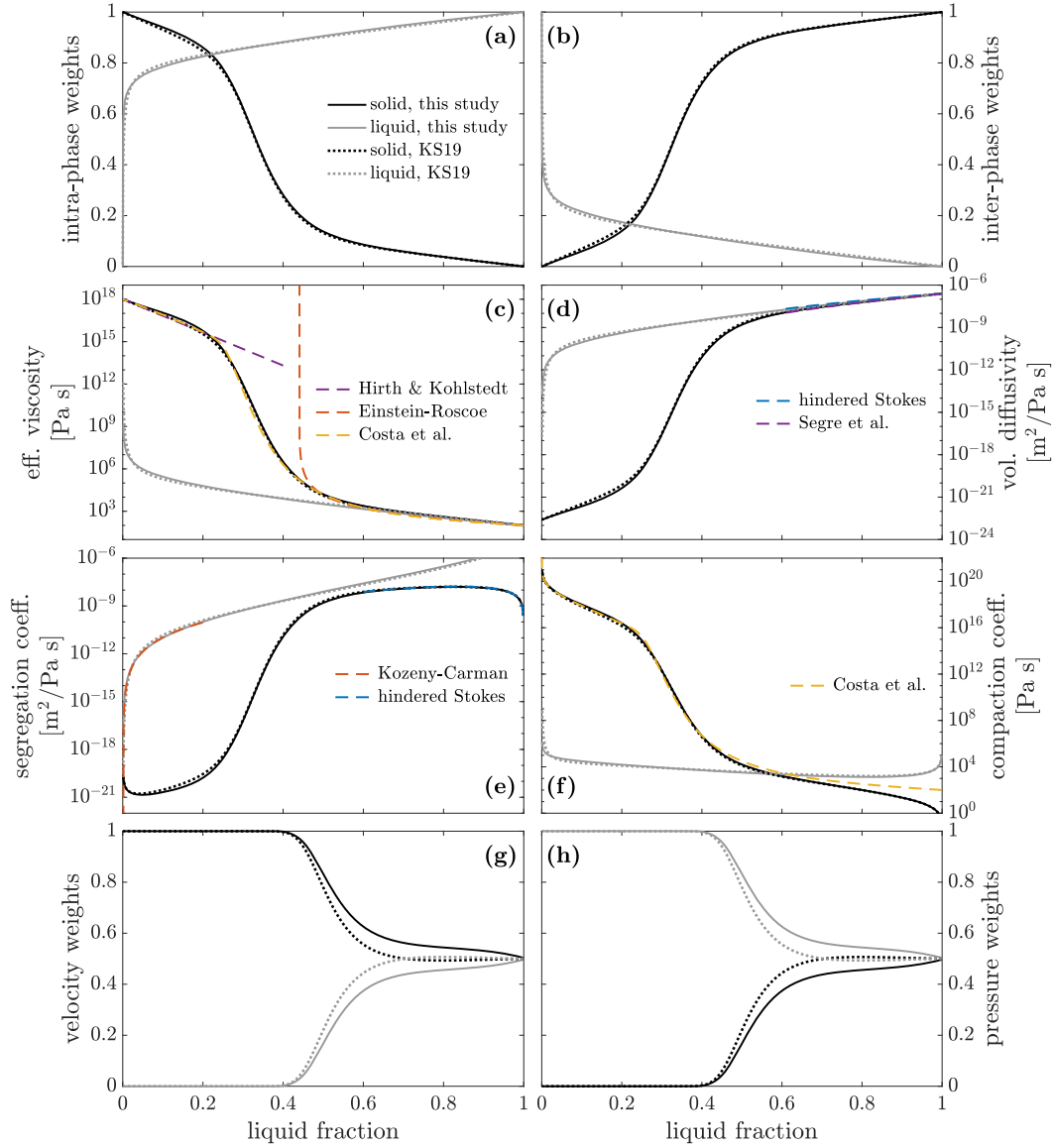


**Figure 1.** Material closures for the two-phase solid–liquid system, calibrated to an olivine–basalt mixture: (a, b) permission weights  $X_{\phi}^{ik}$ , (c) effective viscosity  $K_v^i/\phi^i$ , (d) volume diffusivity  $K_{\phi}^i/\phi^i$ , (e) segregation coefficient  $\phi^i^2/C_v^i$ , (f) compaction coefficient  $\phi^i^2/C_{\phi}^i$ , (g) velocity weights and (h) pressure weights as functions of liquid fraction  $\phi^{\ell}$ . Solid black and grey lines show the calibration using CATMIP in this study, while dotted black and grey lines show the previous calibration from Keller & Suckale (2019). Models used to constrain the parameter estimation are shown in the coloured lines.

$\text{m s}^{-1}$ ,  $10^0 \text{ Pa}$ ,  $10^{-2}$ ], as they appear in the vector  $y^i$ . Both `thtlim` and `cfflim` were set to large values of  $10^{16}$  to render their effect negligible.

With the supplied initial condition of phase fractions, the numerical model solves for consistent velocity–pressure fields with the additional forcing by the analytical residual term evaluated using the sinusoidal solution fields. For several grid resolutions, we evaluate the L2 norm errors between the numerical and analytical manufactured solutions, normalized by the L2 norm of the solution fields (Fig. 3b). The errors are small and decrease with increasing resolution, converging with second-order accuracy as expected for the staggered-grid central differencing scheme used to discretize the governing equations. These results confirm that the numerical algorithm solves the governing equations correctly and that numerical errors should not interfere with the interpretation of the results.

## 5.2 Scalability of the numerical model

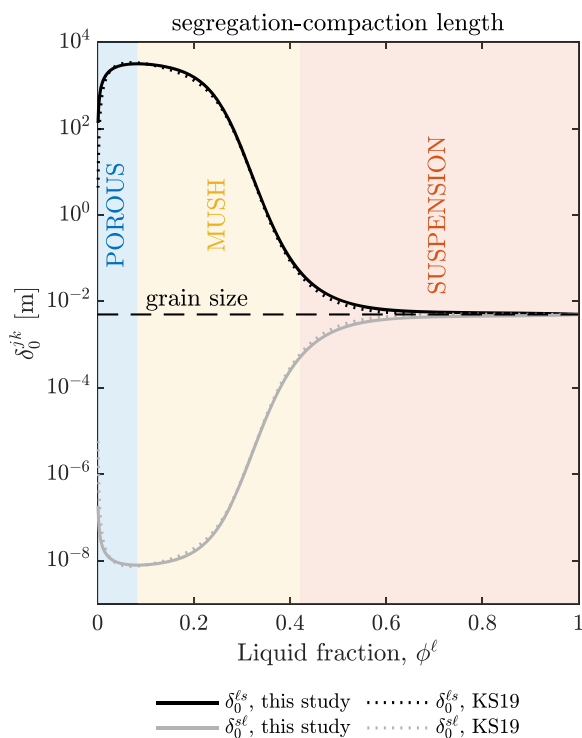
We test the scalability of the model by running simulations at different grid resolutions while recording the number of iterations to convergence and time to solution. We select background phase fractions to represent the suspension and porous flow regimes, while imposing random initial perturbations of amplitude 0.01 and periodic boundary conditions on a square domain of side  $40\delta_0^{ls}$ . We set `thtlim` and `cfflim` to  $10^{16}$  and the iterative step size control  $\alpha$  to 0.95. We run the simulation for one time step, terminating iterations once the absolute residual to the governing equations converges below  $10^{-5}$ . The simulations were run on a standard 2020 8-core Macbook Air with an Apple M1 chip and 16 GB memory.

In the suspension flow regime, we test grid resolutions of  $N^2 = [50^2, 100^2, 200^2, 400^2]$ . The porous flow regime requires a higher grid resolution for accurate solutions, therefore we only test grid resolutions of  $[200^2, 400^2]$ . For each phase proportion, we run two

**Table 1.** Properties for permission functions.

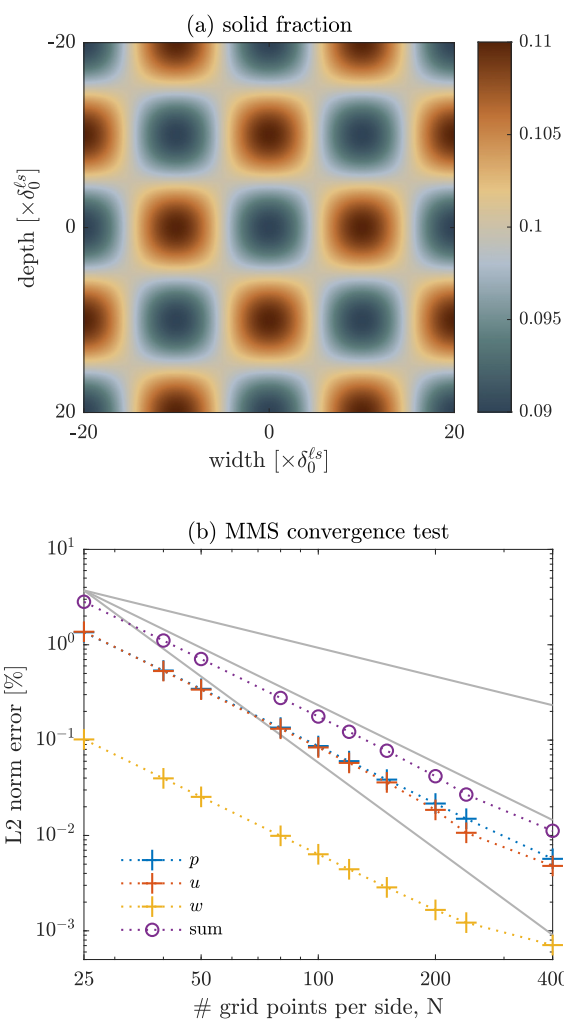
Property	Symbol	Solid	Liquid
Pure-phase properties			
Viscosity [Pa s]	$\eta^i$	$10^{18}$	$10^2$
Granular scale [mm]	$d^i$	5	5
KS19+ calibration of permission weight parameters*			
Slopes	$A$	[0.6945, 0.1832]	[0.5360, 0.1834]
Thresholds	$B$	[0.6906, 0.3094]	[0.9993, 0.0007]
Weights (step width)	$C$	[0.6889, 0.1750]	[0.8154, 1.5642]
CATMIP calibration of permission weight parameters (this study)*			
Slopes	$A$	[0.5989, 0.1772]	[0.0397, 0.1182]
Thresholds	$B$	[0.6870, 0.3130]	[0.9998, 0.0002]
Weights (step width)	$C$	[9.0105, 0.1592]	[0.7249, 3.5524]

+ Keller &amp; Suckale (2019).

\* Permission weight fitting parameters  $A, B, C$  are given as they relate to [solid, liquid], e.g. the order of slope values is  $[A^{ss}, A^{sl}], [A^{ls}, A^{ll}]$ .**Figure 2.** Segregation-compaction lengths  $\delta_0^{ls}$  (liquid segregation, solid compaction) and  $\delta_0^{sl}$  (solid segregation, liquid compaction) for the calibrated two-phase system, compared with the previous calibration from fig. 6 of Keller & Suckale (2019). Background colours show the flow regimes derived using the new calibration.

sets of simulations with different conditions on the damping parameter in the iterative scheme  $\beta$ : one with a fixed  $\beta$  for all grid resolutions, another with the maximum  $\beta$  permitted at a given grid resolution (Fig. 4a). In the former case with fixed  $\beta$ , we use a  $\beta$  low enough to produce stable convergence for all tested grid resolutions. In the latter case with variable  $\beta$ , we use the maximum stable value of  $\beta$  found by trial and error, which makes better use of the pseudo-transient method.

With fixed  $\beta$ , the pseudo-transient iterative solver demonstrates a favourable scaling (blue points in Fig. 4b): as the resolution quadruples, the number of iterations needed increases by less than four times (i.e. below the grey line), as discussed in Section 3.2. With

**Figure 3.** Model verification by the method of manufactured solutions. (a) Solid fraction distribution in the suspension flow regime on a square domain of side  $40\delta_0^{ls}$ . Sinusoidal patterns of the same wavelength are used for the pressure and velocity fields but with different amplitudes and phase shifts. (b) Convergence plot of the L2 norm errors comparing the numerical and analytical solutions for pressure  $p$ , horizontal velocity  $u$  and vertical velocity  $w$  at increasing grid resolution, where  $N$  is the number of gridpoints along one dimension (note logarithmic horizontal axis). The grey lines are, in increasing order of steepness, reference lines for 1st, 2nd and 3rd order convergence.

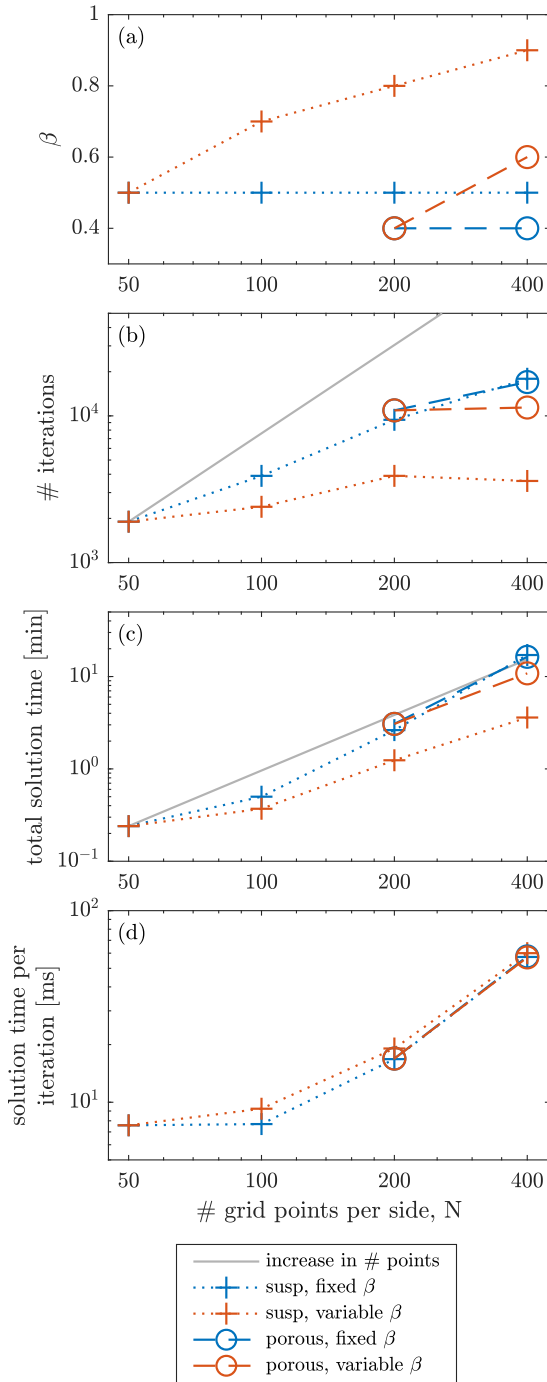


**Figure 4.** Model scalability, tested in the suspension flow regime ( $\phi^\ell = 0.90$ , dotted line with crosses) and in the porous flow regime ( $\phi^\ell = 0.05$ , dashed line with circles) on a square domain of side  $40\delta_0^{\ell s}$ . For each flow regime, we show results using a fixed damping factor  $\beta$  (blue), and using the maximum  $\beta$  for that discretization (‘variable  $\beta$ ’, red). (a)  $\beta$  used in each simulation; (b) number of iterations needed to reach an absolute residual of  $10^{-5}$ ; (c) total solution time in minutes; (d) solution time per iteration in milliseconds. The logarithmic horizontal axis in all plots is the number of gridpoints along one dimension  $N$ . In (b) and (c), the grey line shows a linear scaling that follows the increase in grid resolution.

variable  $\beta$ , the increase in the number of iterations is further curtailed (red points in Fig. 4b). The total solution time for the fixed  $\beta$  case shows approximately quadruple scaling, while the variable  $\beta$  case shows a slightly lower scaling due to the smaller number of iterations (Fig. 4c). For finer grids, each iteration requires more time because of more matrix multiplications to calculate the material closures and constitutive relations, and is not substantially affected by  $\beta$  (Fig. 4d). Even so, finer grids permit larger  $\beta$ , enabling convergence with fewer iterations and overall shorter time compared to the simulations with fixed  $\beta$ . The scalability analysis confirms that the pseudo-transient method scales well and is suited to solving this problem. This result is significant also because formulating an implicit direct solve for the general  $n$ -phase problem would require assembly of a large and relatively dense coefficient matrix compared to previous two-phase porous and suspension models, thus further amplifying the algorithmic complexity and computational cost typical of direct methods (e.g. Keller *et al.* 2013; Birnbaum *et al.* 2020).

## 6 NUMERICAL EXPERIMENTS

### 6.1 Porous flow regime in 1-D: porosity wave trains

Numerous studies have examined the development of porosity waves from porous flow through a deformable matrix based on the compaction model (McKenzie 1984; Katz 2022). Ahead of liquid-rich perturbations, buoyancy-driven liquid overpressure will cause viscous decompaction of the matrix and hence an increase in liquid fraction. At the trailing end of the perturbation, the opposite process occurs: the matrix compacts and liquid is expelled. This gives rise to porosity waves that propagate against gravity faster than the speed of liquid percolation through the pore space (Barcilon & Richter 1986; Scott & Stevenson 1986).

As a qualitative benchmark, we test the emergence of porosity waves from our numerical model using a 1-D permeability barrier test, where a step down to lower liquid fraction is imposed in the direction of liquid percolation (leftmost profile in Fig. 5a). The initial permeability barrier is smoothed for numerical stability. Liquid ascends through the solid matrix due to buoyancy, hence the prevailing flux direction is upward. As the liquid encounters a region of lower liquid fraction, permeability drops and the liquid flux decreases. The solid compaction pressure,  $P_\Delta^s \approx \phi^s(p^s - p^\ell)$ , is initially negative at the barrier because the liquid is at a higher pressure than the solid (Fig. 5b). This definition of compaction pressure follows the convention in Keller & Suckale (2019) which is opposite in sign to that in McKenzie (1984). The liquid decompacts (i.e. volumetrically expands) the solid matrix, causing an accumulation of liquid at the barrier (second profile in Fig. 5a). However, this drains the zone immediately below, leading to matrix compaction and a decrease in liquid fraction there. This forms a new permeability barrier, where liquid accumulates and drains the region immediately below. Successive cycles of decompaction ahead and compaction behind emergent permeability barriers cause a train of porosity waves to develop, similar to those shown in Spiegelman (1993b) and Katz (2022). The wave train is rank-ordered: the wave with the largest amplitude leads successive waves of diminishing amplitude. The porosity wave train mostly propagates upwards but new trailing waves also develop downwards, as shown by the porosity perturbations below the coordinate origin at later times.

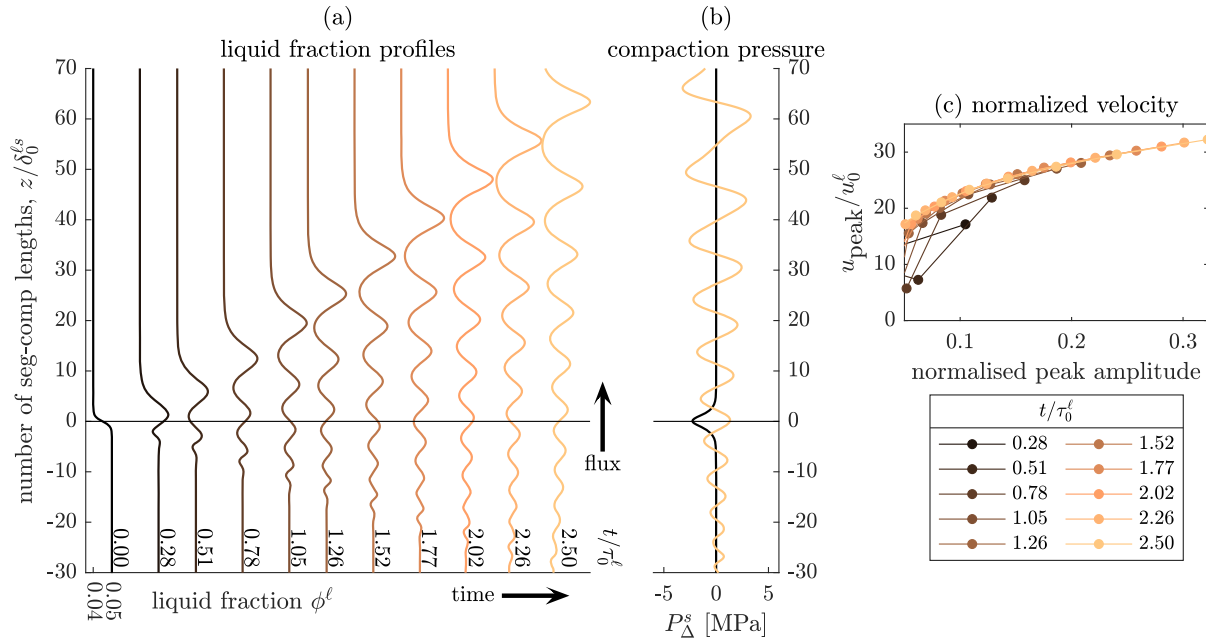


**Figure 5.** 1-D porosity wave trains due to a permeability barrier. Evolution of (a) liquid fraction  $\phi^\ell$ , plotted by time normalized by the liquid percolation timescale  $\tau_0^\ell = 13.4$  kyr. (b) Compaction pressures  $P_\Delta^s \approx \phi^s(p^s - p^\ell)$  of the first and last time step. (c) Normalized velocity of porosity wave peaks against normalized amplitude given by  $(\phi^\ell - 0.05)/0.05$ .

To display the results, we normalize time  $t$  by the liquid percolation timescale,  $\tau_0^\ell = \delta_0^{\ell s}/u_0^\ell$ , where  $u_0^\ell$  is the liquid segregation speed scale (Keller & Suckale 2019),

$$u_0^\ell = \frac{(\phi_0^\ell)^2}{C_{v,0}^\ell} (\rho_0^\ell - \rho_0^s) g_0 \quad (20)$$

using characteristic scales for their respective quantities:  $C_{v,0}^\ell$  is the momentum transfer coefficient calculated at the background liquid fraction  $\phi_0^\ell$  of 0.05,  $\rho_0^\ell$ ,  $\rho_0^s$  are the pure-phase liquid and solid densities, while  $g_0$  is the gravitational acceleration. At the last time step of  $t/\tau_0^\ell = 2.50$  in the figure, the leading wave has advanced  $63\delta_0^{\ell s}$ , which is  $63/2.50 \approx 25$  times faster than the liquid percolating at  $u_0^\ell$ .

Analytical solutions to the compaction equations under idealized conditions permit solitary wave solutions, which are shape-preserving waves that propagate at a constant speed proportional to their amplitude (Scott & Stevenson 1984; Barcilon & Richter 1986; Stevenson & Scott 1991). Our model gives rise to porosity waves; however, these are not strictly solitary waves. Solitary wave solutions require simple power law dependence of compaction viscosity, matrix shear viscosity and matrix permeability on liquid fraction, as well as constant liquid viscosity (Simpson & Spiegelman 2011; Richard *et al.* 2012). The permission functions in the present model do not conform to such idealized material properties, and recasting the model in this form would sacrifice its generality to the other flow regimes. Nevertheless, the shape of the leading wave strongly resembles analytical solitary wave solutions, and the general relationship of higher wave speeds for larger wave amplitudes still holds (Fig. 5c). We normalize peak amplitudes by 0.05, the background liquid fraction below the permeability barrier, and wave speeds by  $u_0^\ell$ , the liquid segregation speed scale. At each time step shown, the rightmost point represents the leading wave, which has the largest peak amplitude and propagates at highest speed. Going leftwards, each subsequent wave is of lower peak amplitude and speed. Over

time, waves grow in amplitude and develop a positive, non-linear amplitude-speed relationship that remains consistent through further time steps. Some small amplitude waves at early time fall below this relationship, which we interpret as incipient waves that eventually grow to follow the common trend.

## 6.2 Porous flow regime in 2-D: porosity wave breakup

To test the emergence of porosity waves in 2-D, we run a simulation in the solid-dominated regime with a horizontal liquid-rich band. The background liquid fraction is 0.04 and the liquid-rich band has a Gaussian shape with a maximum liquid fraction of 0.05, causing it to be buoyant and rise through the domain. Smooth random noise of amplitude 0.0025 is added to provide low-level 2-D perturbations to the otherwise pseudo-1-D initial condition. The rectangular domain is 80 times  $\delta_0^{\ell s}$  at the background phase fraction in the vertical direction, and 40 times in the horizontal direction. The vertical dimension is large enough to ensure that compaction pressures can decay to zero away from the liquid-rich band, while the smaller horizontal dimension reduces computational costs. Periodic boundary conditions are applied on all sides.

The temporal evolution of liquid fraction shows the rise and eventual breakup of the pseudo-1-D liquid-rich band into an approximately spherical 2-D porosity wave (Fig. 6a and Video S1). Time is non-dimensionalized by  $\tau_0^\ell$  at the background liquid fraction as in the 1-D porosity wave simulations. The periodic boundary conditions cause the band to exit the top and enter the bottom of the domain. In the left half of the band, a region with a slightly higher initial liquid fraction due to random perturbations attracts more liquid over time. Since the speed of porosity waves increases with amplitude, the liquid-rich region rises at a faster speed, eventually breaking off from the band at  $t/\tau_0^\ell \sim 4.0$ .

The breakup of a 1-D Gaussian or 1-D solitary wave into approximately 2-D spherical waves was also previously observed



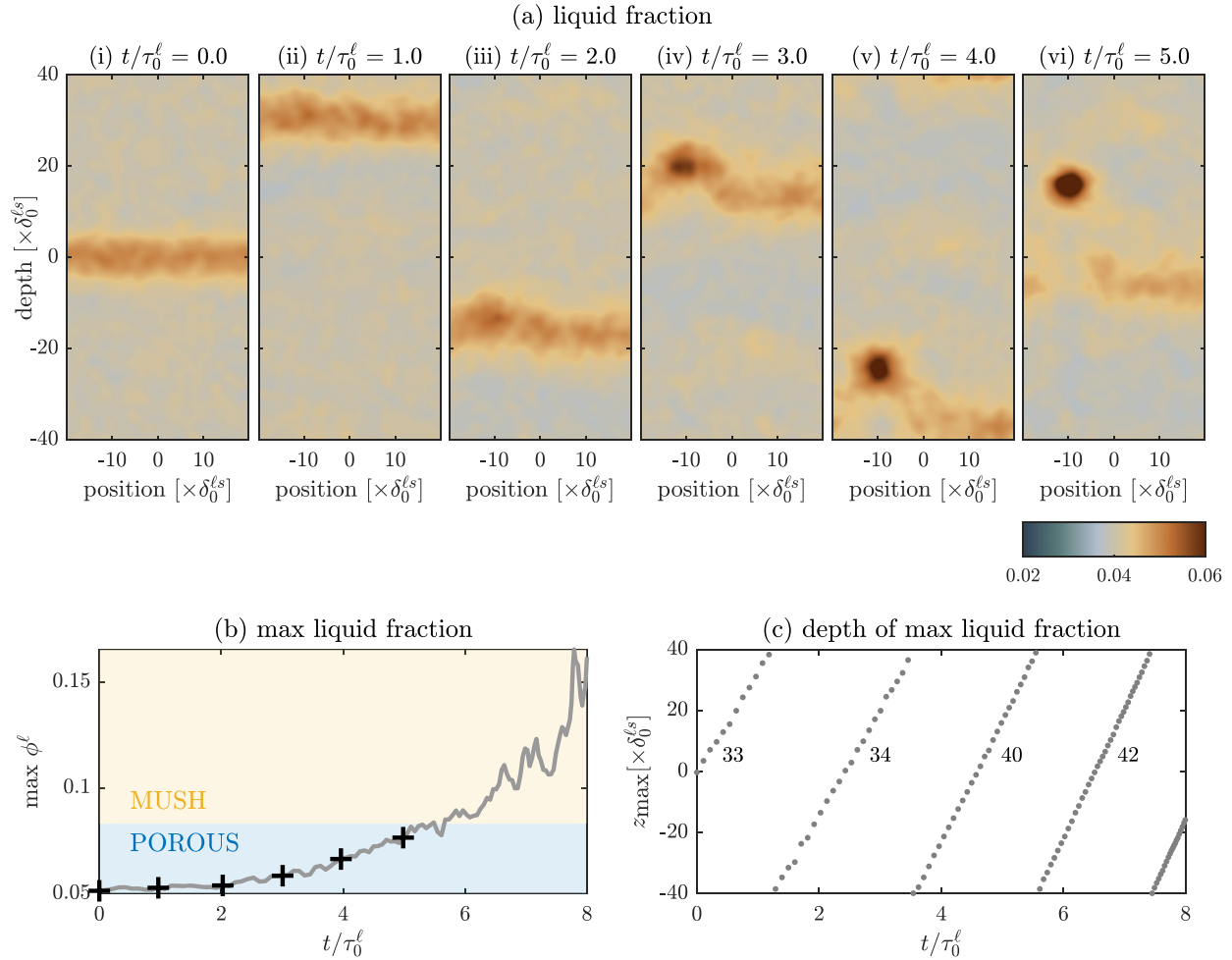


**Figure 6.** 2-D porosity waves with approximately spherical geometry formed by the breakup of a pseudo-1-D liquid-rich band. (a) Evolution of liquid fraction through time, where  $\tau_0^l = 13.4$  kyr, wrapping around in the vertical direction due to periodic boundary conditions. (b) Maximum liquid fraction during the simulation. Background colours denote the liquid fraction corresponding to the porous (blue) and mush (yellow) flow regimes, and black crosses mark the times in (a). (c) Depth of maximum liquid fraction, where the numbers indicate the average velocity over each domain traverse in non-dimensional units ( $\delta_0^{ls}/\tau_0^l$ ).

in Scott & Stevenson (1986). A 2-D analogue (i.e. breakup of a 2-D Gaussian) was observed in Dohmen & Schmeling (2021). While we observe a similar evolution, we note that the emergent wave is not stable over time—it is not a true soliton with a fixed amplitude travelling at a fixed speed, as shown in Barcilon & Richter (1986) and Simpson & Spiegelman (2011). In fact, its maximum liquid fraction increases over time (Fig. 6b), and at a growing rate. This causes a corresponding increase in the speed of the point of maximum liquid fraction (Fig. 6c), from 32 to 43 in non-dimensional units over the four times the wave traverses the domain. Again, this departure from solitary wave solutions arises because we relax the strict assumption of power-law rheology needed to produce solitons (Barcilon & Richter 1986; Simpson & Spiegelman 2011). As a result, liquid accumulates in the perturbation and the flow regime eventually transitions from porous flow to mush flow. Here, strong matrix weakening provides a low pressure region that attracts more melt (Stevenson 1989). Eventually, when the liquid fraction increases to the point that the  $\delta_0^{ls}$  in the liquid-rich region experiences a strong contraction around the solid disaggregation threshold, the simulation grows unstable and diverges.

### 6.3 Suspension flow regime in 1-D: particle concentration waves

In the suspension flow regime, particle concentration waves develop if the solid segregation speed decreases with increasing solid fraction (Manga 1996; Drew & Passman 1999). This behaviour is expected from hindered Stokes settling, where the segregation speed decreases with a power law of solid fraction. Our coefficient model is calibrated to a hindered Stokes settling model with a hindering factor of  $(1 - \phi^s)^5$  (Keller & Suckale 2019). Shock-rarefaction waves should form and lead to a particle ‘traffic jam’ with a sharp tail developing into a shock over time but a widening front or rarefaction where particles can more freely settle into the lower concentration region below.

We qualitatively benchmark the numerical model in this regime by examining the evolution of a solid-rich layer against a uniform background solid fraction of  $\phi^s = 0.05$ . We first describe the expected behaviour by analysing the characteristics of the 1-D governing equations with some simplifying assumptions (following Drew & Passman 1999, section 22.3), then show a set of 1-D numerical simulations using the full set of equations that recover the expected behaviour.

For liquid-dominated systems, assuming that (i) the solid and liquid phases are equilibrated in pressure ( $\Delta P^{i*} \approx 0$ ,  $\Delta(\nabla P)^{i*} \approx 0$ ), (ii) the reference pressure and velocity are equally weighted by each phase (i.e.  $C_v^s \approx C_v^\ell$ , Fig. 2) and (iii) both momentum flux coefficients  $K_\phi^i$  are small and negligible, we can simplify the governing eqs (6) and express the phase velocity difference as

$$v^s - v^\ell = \frac{2\phi^\ell \phi^s (\rho^s - \rho^\ell)g}{C_v^s}. \quad (21)$$

Here we define  $g = -9.81 \text{ m s}^{-2}$ , consistent with the equations in Section 2. Given a denser solid phase,  $v^s - v^\ell < 0$  so that the solid phase settles downwards relative to the liquid. Since each phase is incompressible, the mixture volumetric flux  $\bar{v} = \phi^s v^s + \phi^\ell v^\ell$  must be divergence free and hence a constant to maintain mass balance, therefore we can obtain the velocity of the solid phase as,

$$v^s = \bar{v} + \frac{2(\phi^\ell)^2 \phi^s (\rho^s - \rho^\ell)g}{C_v^s}, \quad (22)$$

Given input values for viscosity, grain size and permission weight parameters  $A$ ,  $B$ ,  $C$ , and under a fixed  $\bar{v}$  to conserve mass, the solid velocity  $v^s$  is purely a function of solid fraction. Thus, we can express the solid mass balance equation as

$$\frac{\partial \phi^s}{\partial t} + \left( v^s + \phi^s \frac{dv^s}{d\phi^s} \right) \frac{\partial \phi^s}{\partial z} = 0. \quad (23)$$

The terms in parentheses on the left-hand side form the characteristics of the solution, along which  $\phi^s$  is a constant. Since  $v^s$  depends only on the solid fraction, the characteristic is constant for a given  $\phi^s$ . For the material properties in this study (Table 1), the characteristics have negative values at  $\phi^s = 0^+$  and increase with solid fraction, becoming positive and reaching a maximum at  $\phi^s = 0.27$ . We focus our analysis on solid fractions below this maximum value to stay well within the suspension flow regime. Applying the characteristics conceptually to a 1-D Gaussian perturbation of higher solid fraction predicts that a shock-rarefaction wave should form over time (Fig. 7a): since the characteristics become less steep with increasing solid fraction, the characteristics converge along the positive  $z$  side of the Gaussian peak, forming a shock, and diverge along the negative  $z$  side, forming a rarefaction. We test our numerical model against this analysis of characteristics using 1-D simulations with solid grain sizes of 1, 2 and 5 mm, which control  $C_v^s$  (Fig. 7b). We remove the constant background flux  $\bar{v}$  from the numerical solution to focus on the evolution of the solid-rich layer. We take snapshots at the same time normalized by the characteristic timescale  $\tau_\xi = \Delta z/v^s$  of the background characteristic (i.e. at solid fraction 0.05), where  $\Delta z$  is the grid spacing and is the same for all three simulations. We display the  $z$ -axis in dimensional units because  $\delta_0^{\ell s}$  differs among the simulations, being close to the respective solid grain sizes. Since  $C_v^s$  depends on the square of the grain size (8c), the characteristic timescale for the 2 and 5 mm simulations are 1/4 and 1/25 of the characteristic timescale for the 1 mm simulation, respectively.

For each grain size, the solid fraction profile steepens on the upper side of the initial layer and spreads out on the lower side, as expected from particulate suspension theory and the analysis of characteristics. Since the velocity difference  $v^s - v^\ell$  (21) is proportional to the square of the grain size through  $C_v^s$ , the peak of the largest grain size simulation has advanced the furthest. The agreement between the equation analysis and the numerical model shows that the effect of the momentum flux coefficient is negligible in the model. Not predicted by the analysis of characteristics is the result that the shock amplitude grows the slowest for the 5 mm

grain size simulation. This effect arises from the volume diffusivity term containing  $K_\phi^s$ , which was omitted in the equations above assuming perfectly equilibrated phase pressures. Larger grain size increases  $K_\phi^s$  (8b), hence enhancing phase diffusion and retarding shock growth. In contrast, the shock in the 1 mm simulation grows very large. These simulations confirm the hypothesis from Keller & Suckale (2019) that the  $K_\phi^i$  term in the mass balance equation acts to diffuse phase fractions and is relevant in the suspension flow limit.

#### 6.4 Suspension flow regime in 2-D: convection

At high liquid fraction, the small segregation-compaction length  $\delta_0^{\ell s}$  on the solid grain scale suggests that mixture convection should dominate dynamics in real magmatic systems on the meter to kilometre scale (Keller & Suckale 2019; Dohmen & Schmeling 2021). The 1-D simulations above are useful for studying phase segregation dynamics; however, to observe mixture convection, we require simulations in 2-D to account for shear stresses. Previous geological observations and numerical models have suggested that denser, crystal-rich regions can form downwellings in the suspension flow regime (Hess 1960; Sparks *et al.* 1984; Culha *et al.* 2020). Notably, Culha *et al.* (2020) showed that mobilization of crystal-rich clusters can be much more efficient than individual grain settling of segregating crystals. We test the evolution of a denser, solid-rich layer ( $\phi^s = 0.10$ ) overlying a less dense, solid-poor region ( $\phi^s = 0.01$ ) in the suspension flow regime. In this gravitationally unstable configuration, the solid-rich layer should sink into the solid-poor region. For collective flow to emerge, we select a large square domain 100 times the background  $\delta_0^{\ell s}$ . At  $\phi^s = 0.01$ , the background  $\delta_0^{\ell s}$  is close to the grain size of 5 mm, giving a domain of 0.5 m. The layer thickness is set as 10 per cent of the domain height. The boundary between the two layers is imposed as a smoothed sinusoid with its trough centred in the domain. Closed boundary conditions are applied to all sides.

With time, the upper, solid-rich layer sinks through the domain, starting at the trough of the sinusoid (Fig. 8a and Video S2). At the same time, a pure liquid layer develops against the top boundary, while a solid-rich layer develops against the bottom boundary. We non-dimensionalize time by the convective timescale  $\bar{\tau}_0 = L/\bar{u}_0$ , where  $L = L_x = L_z$  is the domain length and  $\bar{u}_0$  is the convective speed scale given by

$$\bar{u}_0 = \frac{\Delta \bar{\rho}_0 g_0 \mathcal{L}_0^2}{\bar{K}_{v,0}}, \quad (24)$$

(Keller & Suckale 2019).  $\Delta \bar{\rho}_0$  is the density difference between the two layers,  $g_0$  is gravitational acceleration,  $\mathcal{L}_0$  is the characteristic system size taken as the thickness of the solid-rich layer and  $\bar{K}_{v,0}$  is the mixture viscosity of the lower layer, calculated from the sum of the solid and liquid effective viscosities at a solid fraction of 0.01. By  $t/\bar{\tau}_0 \approx 3.0$ , the initial trough of the perturbation impinges on the lower boundary layer, causing the lower layer to be thinner at the centre and thicker at the edges of the domain. Eventually, by  $t/\bar{\tau}_0 \approx 5.0$ , most of the solids have sunk to the bottom of the domain to form an approximately horizontal boundary layer.

While solids do settle faster within the perturbation, the solid segregation flux is two orders of magnitude smaller than the mixture flux (Fig. 8b). The mixture flux shows a clear convective cell, where the central downwelling is compensated by upwellings along the lateral domain edges (Fig. 8c). Combined, these two panels show that mixture flow dominates dynamics in this simulation. The relatively

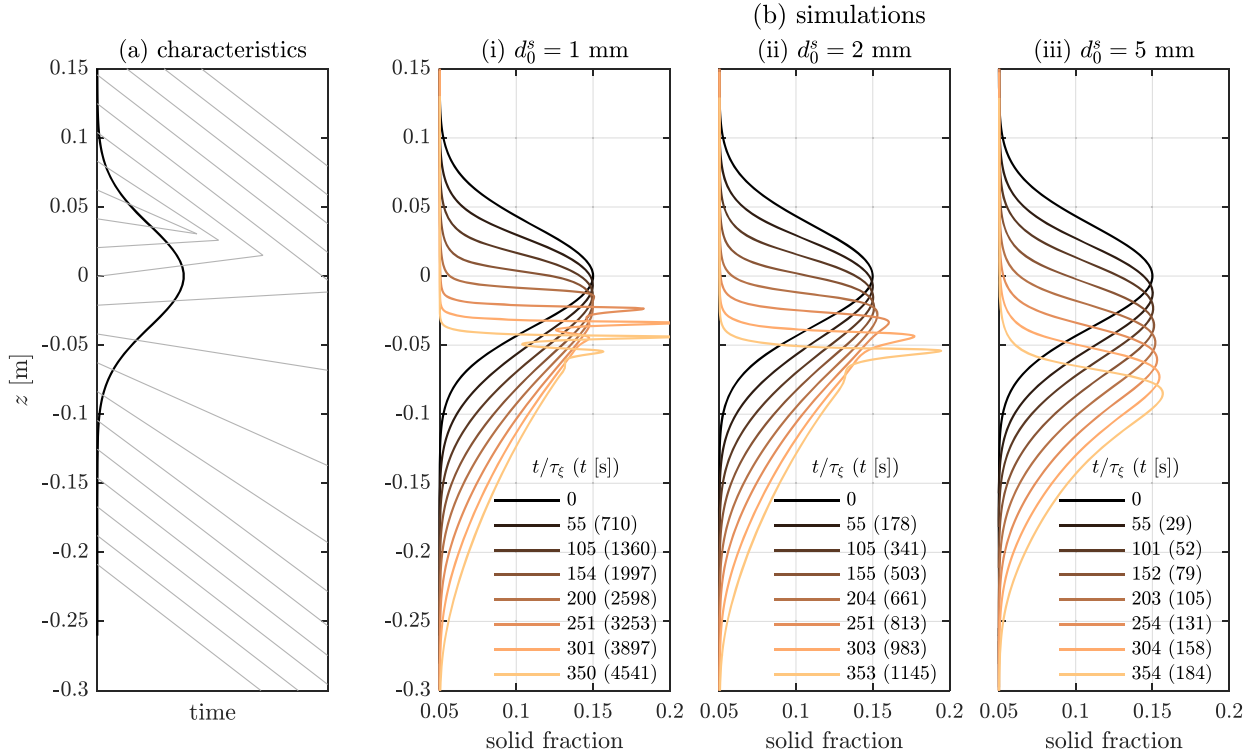


**Figure 7.** 1-D particle concentration waves in the suspension flow regime formed from a solid-rich perturbation. (a) Characteristics (thin grey lines) for the input Gaussian solid fraction profile (thick black line), showing a shock forming on the positive  $z$  side of the peak and a rarefaction forming on the negative  $z$  side. (b) Profiles of solid fraction for grain sizes [1,2,5] mm from numerical solutions initialized by a background solid fraction of 0.05 and a Gaussian perturbation of amplitude 0.1. Profiles are adjusted by the background flux  $\bar{v}$ . Snapshots are at approximately the same normalized time  $t/\tau_\xi$  using the background characteristic timescale, with time in seconds shown in parentheses ( $\tau_\xi = [13.0, 3.24, 0.519]$  s).

minor solid settling only becomes evident against the impermeable lower boundary of the domain where the solids accumulate. Even here, mixture flow affects its morphology, as the outwardly oriented mixture flux vectors drive solid accumulation towards the outer edges of the domain. The minor role of solid settling is also shown in the higher solid fraction on the trailing, upper edge of the perturbation, as predicted by the 1-D particle concentration waves (most clearly seen in panel 8 a(ii)). However, shock formation is circumvented because the 2-D setup allows mixture convection to circulate the solid particles. A similar effect is observed even for the simulations with smaller grain size, where the shock is stronger. Therefore, particle concentration waves are not likely to play an important role in real magmatic systems, whose liquid-rich regions will typically be larger than the simulation domain (0.5 m).

### 6.5 Mush flow regime in 1-D: liquid localization

The model extends self-consistently into the mush regime. The topology of the segregation-contraction length  $\delta_0^{\ell s}$  (Fig. 2) suggests that melt localization will become prominent in the mush regime, consistent with previous analyses of weakening matrix rheology from Stevenson & Scott (1991). Regions with locally higher liquid fraction will have lower pressure and attract more liquid, while also becoming smaller in scale (Keller & Suckale 2019). For example, from the disaggregation threshold of 0.31, increasing the liquid fraction by 0.10 contracts  $\delta_0^{\ell s}$  by about a factor of 200.

The substantial contraction in  $\delta_0^{\ell s}$  can cause problems with numerical resolution. At initialization, the grid size is defined such that several grid cells resolve one  $\delta_0^{\ell s}$ , calculated at the initial phase

proportion. As the simulation proceeds, liquid localizes and concentrates on positive perturbations in liquid fraction, thus decreasing the local  $\delta_0^{\ell s}$  there. As localization intensifies over time, salient flow features may go below the grid size and cause solutions to diverge. To mitigate this problem, the permission function limiter `thtlim` caps the maximum range of permission function values within each phase and thus dampens the intensity of localization. Both limiters were previously set to high values  $\geq 10^6$  for the porous and suspension flow experiments, however here they play an important role.

We test model performance in the mush regime using a 1-D setup with a positive, Gaussian-shaped liquid perturbation of amplitude 0.02 above the background liquid fraction of 0.30 (Fig. 9a, dotted line). Periodic boundary conditions are imposed on a domain that is 100 times the background  $\delta_0^{\ell s}$ , equivalent to 3.4 km, comparable to the likely size of crustal mush bodies. Since the model is run in the pseudo-1-D mode, we can use a fine grid resolution, here 80 grid cells per  $\delta_0^{\ell s}$ . We systematically run models with different values for `thtlim` until they diverge. For models with large limiters ( $\geq 10^6$ ), we set both `thtlim` and `cfflim` to the same value. For models with small limiters, we set `thtlim` to  $10^2 - 10^5$  while keeping `cfflim` at  $10^6$ . Other numerical solution parameters ( $\alpha$ ,  $\beta$  for the iterative solver, CFL criterion, absolute and relative tolerances) are kept the same for all simulations.

With a smaller value of `thtlim`, the simulations can be run to longer time (Figs 9a and b). All the simulations with `thtlim` and `cfflim` greater than or equal to  $10^8$  show indistinguishable results at the time when the solutions diverge around  $t/\tau_0^l = 4.5$  (Fig. 9a). There are slight differences in the final times consistent with the trend of longer time for smaller `thtlim`, but only at the

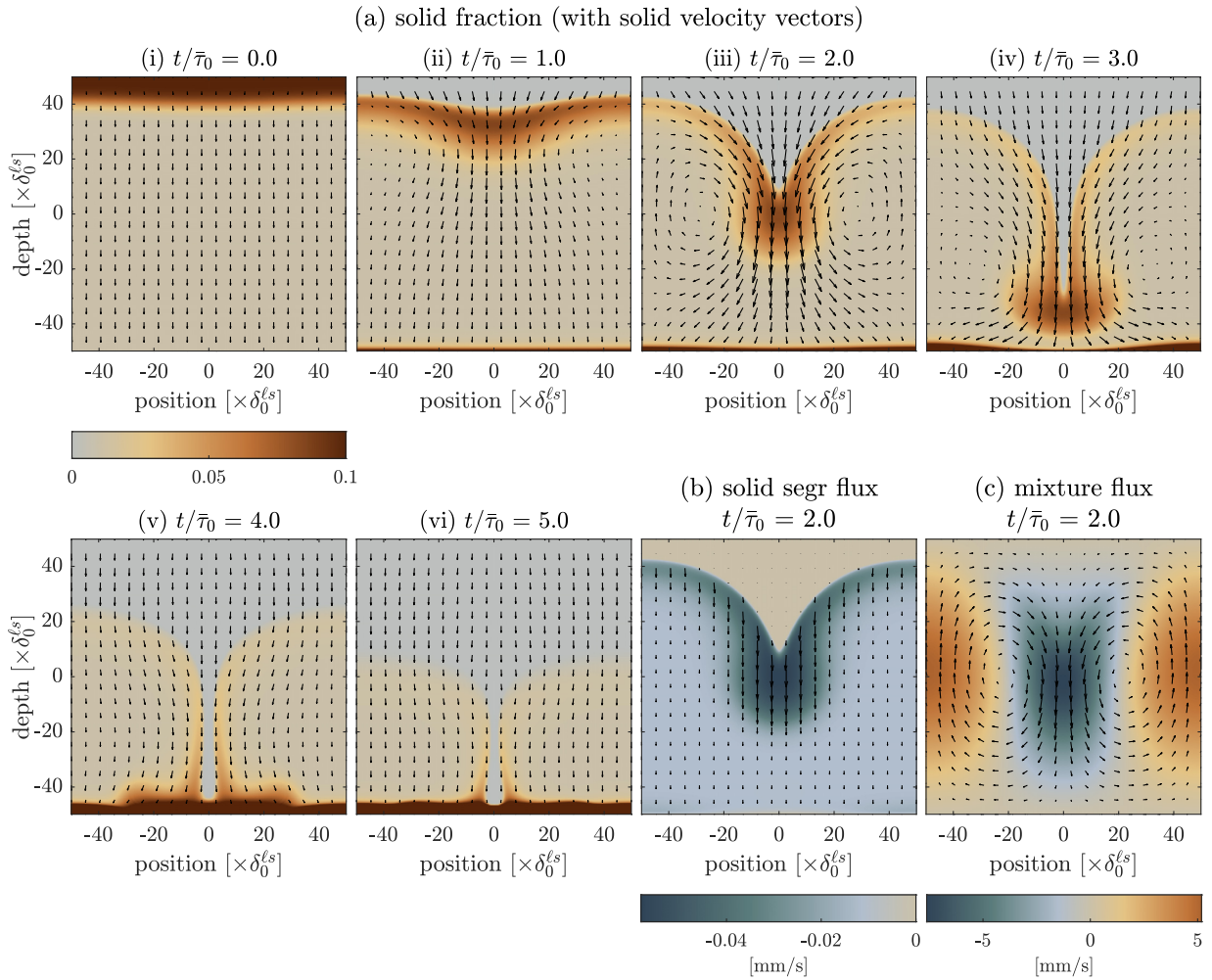


**Figure 8.** 2-D mixture convection in the suspension flow regime caused by a negatively buoyant top layer ( $\bar{\tau}_0 = 46.9$  s). The top layer with higher solid fraction  $\phi^s = 0.10$  (denser) overlies a region of lower solid fraction  $\phi^s = 0.01$  (less dense). Closed boundary conditions are applied on all sides. (a) Evolution of solid fraction through time overlain with solid velocity vectors. (b) The solid segregation flux  $\phi^s(\mathbf{v}^s - \mathbf{v}^*)$  and (c) mixture flux  $\sum_i(\phi^i \mathbf{v}^i)$  at  $t/\bar{\tau}_0 = 2.0$ . Background colours show the vertical component of the fluxes, while vectors show both horizontal and vertical components.

3rd significant figure. Below  $10^8$ , stabilization of the simulations to longer time is more apparent, even as the liquid peak grows. However, too small a `thtlim` ( $\leq 10^3$ ) significantly affects system dynamics and delays localization by preventing the strong decrease in the solid effective viscosity, as shown in the broader peaks in Fig. 9(a) and the change in slope of the maximum liquid fraction in Fig. 9(c).

During the simulations,  $\delta_0^{\ell s}$  decreases by at least one order of magnitude (Fig. 9d). Longer simulations cause even greater contraction, down to a minimum of  $2.6 \times 10^{-3}$  when `thtlim` is set to  $10^2$ , due to the greater increase in maximum liquid fraction. These simulations suggest that `thtlim` can be reduced to around  $10^4$  to maximize the simulation time while still capturing the essential dynamics.

## 6.6 Mush flow regime in 2-D: stress-driven alignment of liquid-rich bands

To further demonstrate how liquid-rich regions develop in the mush regime, we run a 2-D simulation, again at a background liquid fraction of 0.30. 2-D simulations reveal the interplay between collective

flow and phase segregation, as discussed in the 2-D suspension flow simulations (Section 6.4). Furthermore, previous studies showed that, in the case where the matrix strongly weakens with increasing liquid fraction, the growth of localized, liquid-rich bands aligns with the principal stress directions in the solid matrix (Stevenson 1989; Katz *et al.* 2006; Golabek *et al.* 2008).

We choose a setup representing the rise of a buoyant liquid-rich region in a large magmatic system, and observe the emergence of liquid-rich bands. The domain is a square box with length  $40\delta_0^{\ell s}$  at the background liquid fraction of 0.30 with periodic boundary conditions. Compared to simulations in the porous and suspension flow regime, we are limited in the choice of domain size because a large number of grid cells is needed to compute the solution when liquid localizes; in this example  $N_x = N_z = 600$ . In the centre of the domain, we impose a Gaussian-shaped, liquid-rich perturbation of amplitude 0.01 and width (equivalent to the standard deviation of the Gaussian function) that is 1/8 of the domain length. Low-level 2-D random perturbations of amplitude 0.002 are superposed to initiate localization. Based on the 1-D mush flow analysis in the previous section, we select `thtlim` =  $10^4$  and `cfflim` =  $10^6$  to ensure that liquid localization is well resolved while still permitting simulations to reasonably long times.



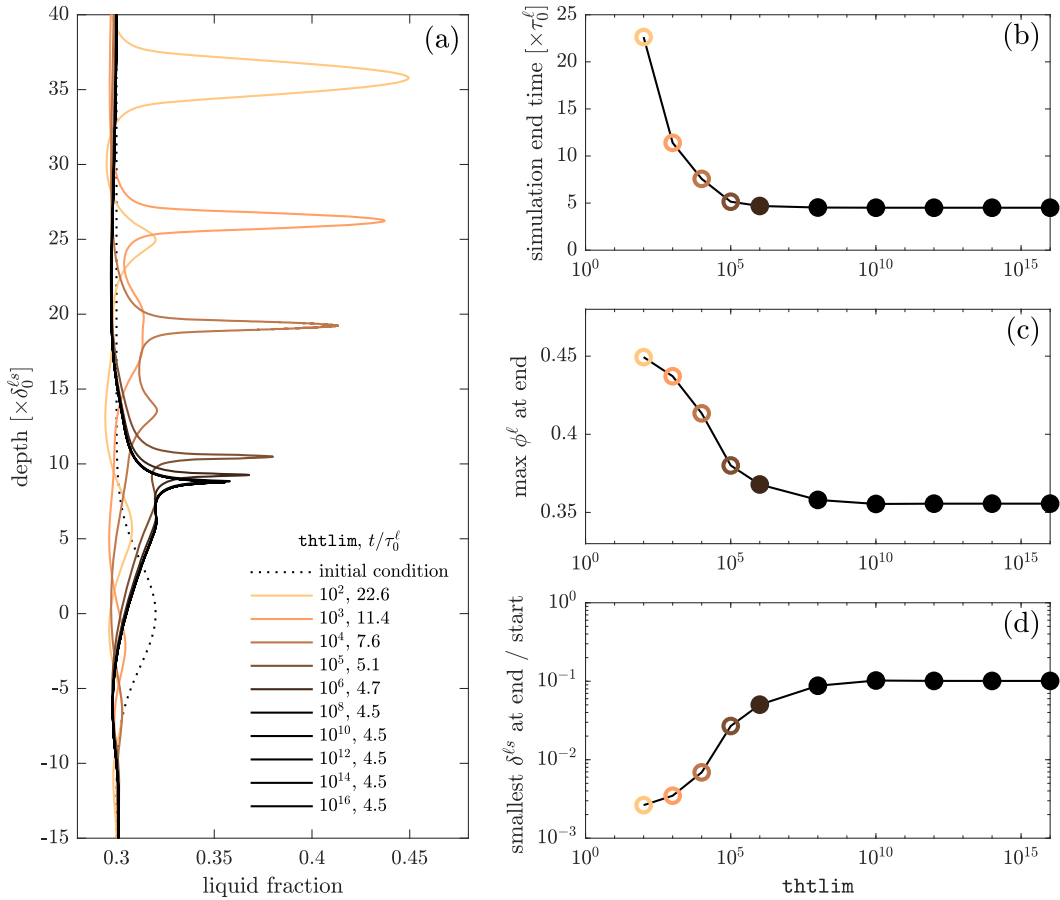


**Figure 9.** 1-D liquid localization in the mush flow regime, requiring the permission function limiter  $\text{thtlim}$  to stabilize simulations at long times. (a) Depth profiles of liquid fractions for a given  $\text{thtlim}$  at the last simulation time step before solutions diverge, normalized by the segregation timescale  $\tau_0^\ell = 0.40$  yr. Profiles for  $\text{thtlim} \geq 10^8$  are indistinguishable and all plotted in black. Summary of results for the (b) simulation end time, (c) maximum liquid fraction at the simulation end time and (d) ratio of the smallest segregation-compaction length  $\delta_0^{\ell s}$  at the simulation end time to the start. Colours have the same meaning as (a). Filled circles indicate that the same value is used for  $\text{thtlim}$  and  $\text{cflim}$ , while open circles indicate that  $\text{thtlim}$  is smaller than  $\text{cflim}$ .

Over time, the central liquid-rich region rises through the domain due to buoyancy (Fig. 10a and Video S3). Since the boundaries are periodic, the liquid-rich region rises, eventually exiting the top and re-entering at the bottom of the domain. The perturbation traverses the domain twice in the time span shown; the perturbation takes  $t/\tau_0^\ell \sim 7.5$  for one domain length traverse. The liquid velocity vectors show diapiric rise of the perturbation, where a central upwelling is compensated by downwellings at the lateral domain edges. Over time, liquid-rich bands develop, radiating out from the top of the Gaussian perturbation. The initial random perturbations also develop into aligned, liquid-rich bands, some of which continue to accumulate liquid over time. This depletes the liquid content of the background mush outside the channels, as shown by the bluer colours relative to the initial condition.

The distribution of stress and strain rate of the solid phase explain the orientation of the liquid-rich bands. Since the matrix is weakened by liquid, we expect the liquid-rich bands to show localization of shear strain rate, while previous analyses suggest the liquid-rich bands orient approximately normal to the least compressive stress direction (Stevenson 1989; Holtzman *et al.* 2003; Katz *et al.* 2006). Fig. 10(b) shows the deviatoric strain rate magnitude and principal stress orientations of the solid matrix. Background colours show the magnitude of deviatoric strain rate tensor calculated from the square root of its second invariant, that is  $\sqrt{\text{trace}(\underline{\underline{D}}^2)}/2$ . The neutral

colour of the colour bar is selected at the mean deviatoric strain rate. Black bars show the least compressive stress direction.

Regions of high deviatoric strain rate coincide with the main liquid-rich region and the liquid-rich bands, with the bands in the domain's upper left corner showing the highest strain rate. At the same time, the perturbation induces a coherent stress distribution as a consequence of the diapirism. Ahead of the perturbation, the least compressive stress direction is oriented concentrically around the perturbation. Behind the perturbation, the least compressive stress is oriented radially outward from the perturbation. The liquid-rich shear bands appear approximately perpendicular to the least compressive stress directions. Furthermore, their formation causes deflections in the otherwise coherent stress field, as shown in the upper left of the domain. Therefore, this simulation shows that the mush flow regime favours the formation of localized, liquid-rich shear bands aligned almost normally to the least compressive stress direction.

### 6.7 Three-phase suspension flow in 2-D

Given the  $n$ -phase general implementation, the model can easily be applied to mixtures with more than two phases if provided with suitable permission functions, which we have shown is not a trivial task

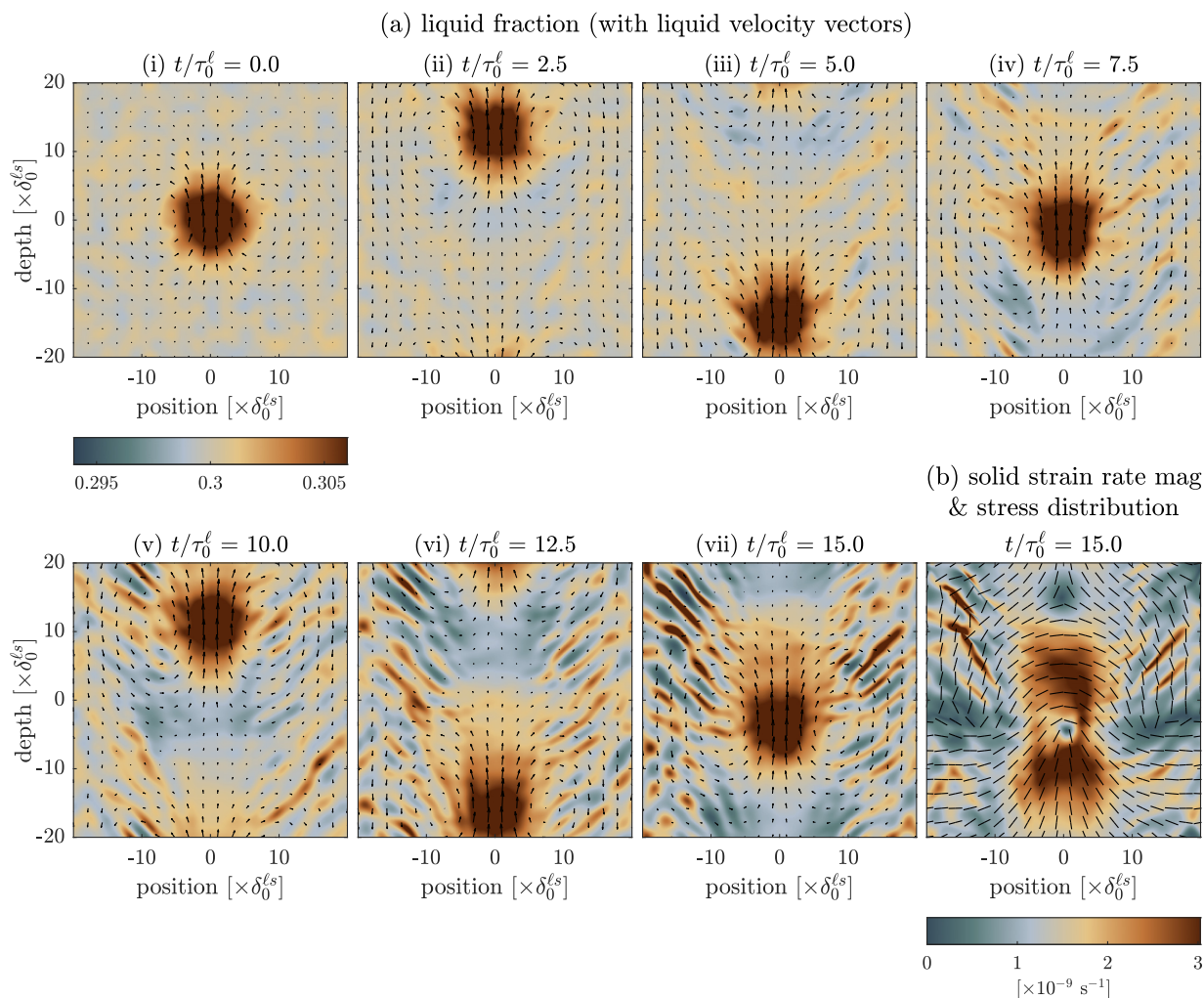


**Figure 10.** 2-D liquid localization in the mush flow regime, forming liquid-rich bands. The initial condition consists of a background liquid fraction of 0.30 with a central Gaussian-shaped, liquid-rich perturbation of amplitude 0.01 and smaller random perturbations of amplitude 0.002. (a) Evolution of liquid fraction through time normalized by the segregation timescale  $\tau_0^\ell = 0.40$  yr, overlain with liquid velocity vectors. (b) Deviatoric strain rate magnitude of the solid phase at the last time step shown, overlain with bars showing the least compressive stress direction.

even for two-phase mixtures. We demonstrate a three-phase example comprising solid crystals, liquid melt, and a magmatic volatile phase (MVP) using conceptually based permission functions. We use the same solid and liquid properties as in the two-phase case above, while defining the MVP as an incompressible, low density, low viscosity fluid ( $\rho^f = 200 \text{ kg m}^{-3}$ ,  $\eta^f = 10^{-3} \text{ Pa s}$ ,  $d^f = 5 \text{ mm}$ ). Quantitatively calibrating the permission functions using experiments and theory will be the subject of a future study. The current permission functions (Fig. A1 in Keller & Suckale 2019) rely on two guiding principles that supplement the two-phase case. Compared to the liquid phase, the MVP is less wetting on the solid (i.e. larger dihedral angle), and therefore has a higher percolation threshold in a solid-dominated matrix. Furthermore, the MVP can form foams—disconnected bubbles with thin melt films—thus the sharp increase in MVP connectivity should occur at a higher MVP fraction in a liquid-dominated mixture.

We demonstrate the three-phase flow problem on a 2-D domain in the suspension flow limit with a setup similar to the two-phase problem in Section 6.4. We simulate the convective instability of a low-density layer along the base of the domain, as might apply if a volatile-rich magma enters a magmatic system from below.

The domain has a background solid, liquid and MVP fraction of [0.05, 0.94, 0.01]. The low density layer has a lower liquid fraction and higher MVP fraction, [0.05, 0.90, 0.05]. We use a closed, square domain of size 100 times the largest segregation-compaction length, equivalent to 0.5 m. At the background phase proportion, the largest segregation-compaction length is  $\delta_0^{\ell s}$ , corresponding to liquid segregation and solid compaction as in the two-phase cases.

Over time, the low density layer forms a convective instability rising through the domain, depleting the MVP fraction along the base (Fig. 11 and Video S4). We observe convective cells in the solid and liquid velocity fields, where a central upwelling is compensated by downwelling along the sides of the domain [panels (i)–(iii)]. The convective cell is less pronounced in the MVP velocity field because its strong buoyancy causes upward flow to dominate. Nevertheless, slight deflections in the MVP velocity field promotes inward concentration of MVP towards the central upwelling.

The addition of a third phase results in more complex phase segregation dynamics. In the solid phase, the front of the instability shows a slightly higher solid fraction because the upward migrating convective cell encounters downward settling solid grains [Fig. 11 a(iv)]. The liquid phase, having an intermediate density to the solid

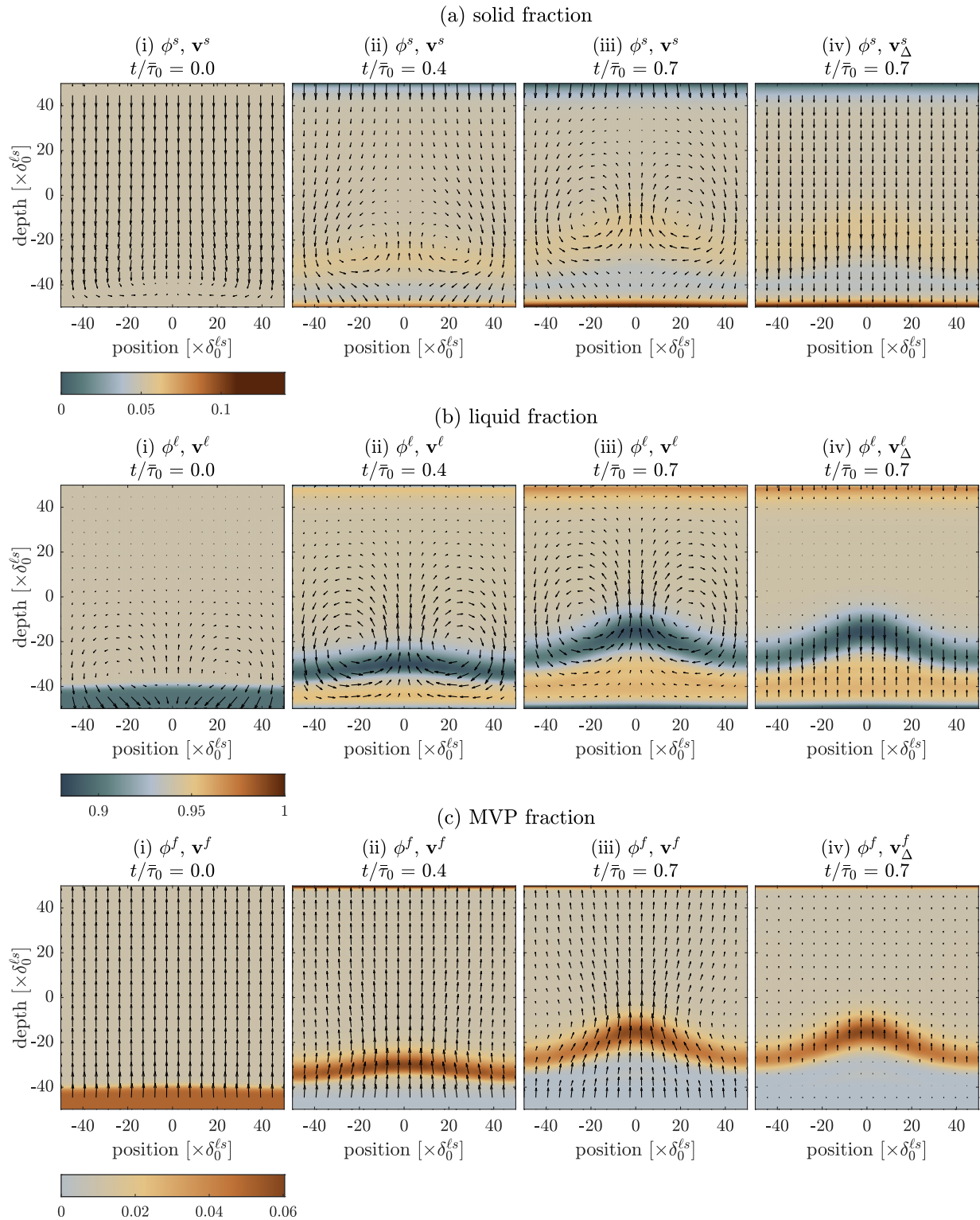


**Figure 11.** 2-D mixture convection of a three-phase magma at high liquid fraction (suspension flow limit,  $\bar{\tau}_0 = 30.6$  s). The background solid, liquid and MVP fractions are [0.05, 0.94, 0.01]. A buoyant layer with lower liquid fraction and higher MVP fraction [0.05, 0.90, 0.05] is imposed at the bottom of the domain. Temporal evolution of (a) solid fraction, (b) liquid fraction and (c) MVP fraction. Panels (i)–(iii) have the respective phase velocity vectors overlain, while panel (iv) shows the last time step again with the respective phase segregation flux  $\mathbf{v}_\Delta^i = \phi^i(\mathbf{v}^i - \mathbf{v}^*)$  overlain.

and MVP phases, displays both positive and negative segregation velocities [Fig. 11 b(iv)]. Within the MVP-rich upwelling, the liquid phase compacts downward and the MVP segregates upward [Fig. 11 c(iv)], while immediately below, where the MVP is depleted, the liquid phase segregates upward to compensate for the settling solid phase. This role reversal of the liquid phase, compensating either for the rise of MVP bubbles or the sinking of crystals depending on phase fractions, suggests that complex multiphase dynamics may be understood as the superposed behaviour of segregating and compacting phase pairs. Huber & Parmigiani (2018) make similar observations in their three-phase model formulated in the porous flow limit.

Outside the convective instability, a solid-poor but liquid and MVP-rich boundary layer forms at the top of the domain, while a solid-rich but liquid and MVP-poor layer forms at the bottom. The thicknesses of the boundary layers are not the same. At the top of the domain, the MVP-rich layer is very thin while the liquid-rich layer immediately below is broader. Continued phase segregation proceeds in this liquid-rich layer so that the MVP forms a highly enriched, thin layer against the top boundary.

The MVP layer eventually goes below the grid resolution and the solutions diverge, similar to the behaviour in the 1-D mush simulations (Section 6.5). This result highlights a key challenge in modelling three-phase, and in general  $n$ -phase, flows of resolving multiple segregation-compactness lengths, which can differ by orders of magnitude. At the beginning of this simulation,  $\delta_0^{f\ell}$ , which describes the MVP segregation-liquid compactness length, is 0.4 of  $\delta_0^{fs}$ , while  $\delta_0^{fs}$ , which describes MVP segregation-solid compactness, is even smaller at  $0.03\delta_0^{fs}$ . As MVP accumulates along the top of the domain,  $\delta_0^{f\ell}$  decreases and causes the upper MVP boundary layer to become thinner. The small  $\delta_0^{fs}$  does not appear to affect solutions because of the small solid and MVP fractions. Resolving all three evolving length scales with a reasonable number of grid cells is challenging for this numerical model setup, and can cause solutions to diverge when a segregation-compactness length goes below the grid resolution. Even reducing the limiters below  $10^6$ , the value applied in this case, does not enable markedly longer simulations, suggesting that introducing multiple segregation-compactness lengths increases the numerical complexity of the problem compared to the two-phase mush case.

## 7 MODEL LIMITATIONS

The numerical model presented in this study is suitable for exploring multiphase dynamics of igneous systems under specific conditions and assumptions. Here we discuss the computational limitations of the model. We leave the discussion on conceptual limitations arising from omitted physical and chemical complexities to be found in Keller & Suckale (2019). While the numerical model applies across all phase fractions and flow regimes, the time and length scales on which the model can robustly and efficiently operate are limited.

First, the numerical model was developed to study dynamics up to  $\sim 100$  times the segregation-compactness length, where the interplay between phase segregation and mixture flow is prominent. Consequently, the domain size and grid length are chosen relative to the largest segregation-compactness length at the initial background phase fractions. The numerical time steps are restricted by the largest volume flux or transfer rates. The model is not well-suited to study flow scenarios outside these length and timescales, for example the suspension flow regime on scales larger than tens of metres and longer than centuries, as might arise in large igneous intrusions or

during the magma ocean stage of planetary formation, for example. Such systems would require an intractably large number of grid cells and time steps. Instead, such scenarios are well approximated by a reduced model describing convective flow with hindered Stokes settling and equilibrated phase pressures (e.g. Gutiérrez & Parada 2010; Molina *et al.* 2012; Birnbaum *et al.* 2020).

Second, the wide range of segregation-compactness lengths does not permit a single simulation to span phase fractions in the porous, mush, and suspension flow regimes while sufficiently resolving segregation and compaction processes everywhere. With the calibrated transfer coefficients in this study, the liquid segregation-solid compactness length  $\delta_0^{fs}$  spans 6 orders of magnitude, from the solid grain size of 5 mm to the maximum of 3.4 km at  $\approx 0.08$  liquid fraction. Since a few grid cells are required to resolve each  $\delta_0^{fs}$ , it is not practically feasible to perform a simulation of size 10–100 times  $\delta_0^{fs}$  in the porous flow regime while resolving the smallest length scale in the suspension flow regime on the same numerical grid. As an example, resolving a 10 km domain with 1 mm grid step requires  $10^7$  grid cells along one dimension. Instead, specific model dimensions should be chosen around the phase fractions of interest to explore flow dynamics given a system length scale. Subsequently, results can be compared with simulations at other phase fractions using the same numerical model, as presented in this study.

The problem of scales is most pronounced in the mush regime, where transport coefficients and thus  $\delta_0^{fs}$  span many orders of magnitude over a small range of phase fractions, necessitating the limiters to stabilize the numerical model (Section 3.4). All numerical models addressing the mush regime have to confront this problem of large variations in transport coefficients, typically by introducing a lower or upper cut-off viscosity. While the tests in the end-member porous and suspension flow regimes permit good convergence with the limiters set to large values ( $\geq 10^6$ ), tests in the mush regime show that `thtlim` needs to be reduced to achieve good convergence and longer simulations (Sections 6.5 and 6.6). `thtlim` crucially controls the range of the solid phase effective shear viscosity  $K_v^s$ , which changes by orders of magnitude at the disaggregation threshold. A lower `thtlim` limits this variation in  $K_v^s$ . However, too small a `thtlim` ( $\leq 10^3$ ) alters the system dynamics and delays liquid localization because the matrix does not become as weak in the melt-rich region. Based on these tests, we find a ‘sweet spot’ of `thtlim` around  $10^4$  and `cfflim` at  $10^6$  to ensure that the essential physics are adequately resolved while enabling simulations to progress despite strong localization. In theory, increasing the number of grid cells should allow larger permission function and coefficient contrasts by resolving the localization features; however, in practice we cannot increase the number of grid cells by orders of magnitude while maintaining reasonable computation times. Further model applications to three-phase systems will likely encounter similar challenges due to the presence of multiple segregation-compactness lengths that can differ by orders of magnitude. These models may further require a reduced `cfflim` for solution convergence. In many cases, it will be justified to instead formulate simplified models in limiting cases, which will avoid the need to resolve several of the  $n(n-1)$  inherent length scales of an  $n$ -phase problem.

Third, we recognize that the continuum assumption on which the model is based cannot be applied in the suspension flow regime, at least not in the volume-averaging sense. With  $\delta_0^{fs}$  reduced to the solid grain size and the requirement that each  $\delta_0^{fs}$  be resolved by several grid cells, the discrete grid spacing falls below the solid grain size. This violates the traditional form of the continuum assumption, where each grid cell is conceptualized as a representative volume element containing a large number of local-scale phase constituents



whose behaviour is described by volume averaging to the continuum scale. However, an alternative approach to continuum mixture theory affirms the validity of the governing equations in the suspension regime as it interprets continuum phase fields in terms of ensemble averaging (Drew & Passman 1999; Oliveira *et al.* 2018). Instead of requiring each grid cell to be a representative volume element, the ensemble averaging approach understands each point on a continuum field as representing an average of many physically possible realizations of microscopic phase topology and phase interactions. Hence, a grid cell much larger than the grain scale is not a necessary condition for the model to be valid. The agreement between simulations and existing end-member models (Section 6.3) confirms that our model produces the expected dynamic behaviour. Future comparisons with direct numerical simulations that resolve phase interactions at the granular scale (e.g. Qin & Suckale 2017; Culha *et al.* 2020) may provide a way to further validate the results in this regime.

Finally, some limitations arise from the specific choices of time stepping and spatial discretization for the model. Despite showing good scalability to solve reasonably high-resolution 2-D simulations (i.e.  $\sim 600 \times 600$ ) on a standard personal computer, the present implementation is limited by its serial algorithm. The selected pseudo-transient method is well-suited to parallelization for GPU computing, which has the potential to greatly enhance model efficiency and enable more detailed investigations into fluid localization phenomena (Räss *et al.* 2019, 2022). Improvements on the trial-and-error approach to choosing the damping parameter  $\beta$  by using insights from the governing equations will further enhance model performance (Wang *et al.* 2021).

## 8 CONCLUSION AND FUTURE DIRECTIONS

In this study, we have developed a unified numerical modelling approach based on the theory of Keller & Suckale (2019) to study the fluid mechanics of multiphase magma mixtures. We have verified and calibrated a two-phase, solid–liquid case against experiments and theory on olivine–basalt mixtures. We demonstrated that the numerical model recovers well-known solutions in the porous and suspension flow regimes, while extending analyses into the intermediate mush flow regime and to mixtures with larger number of phases. The numerical model is most suitable for exploring flow dynamics on domains a few times up to 100 times the largest segregation–compaction length and at small phase fraction perturbations around the initial values.

In terms of future model applications, the model's strength is to enable internally consistent investigations of two-phase dynamics across the porous, mush and suspension flow regimes. One goal is to use the model to develop robust and well-justified ways to extend end-member porous and suspension flow models beyond their limited range of phase fractions. Another major goal of future work is to elucidate mush dynamics in light of growing evidence that crustal magmatic systems spend a large portion of their lifetimes in a mush state (Caricchi & Blundy 2015; Sparks *et al.* 2019). Resolving mush dynamics will improve estimates of the melt extraction timescale to assemble eruptible magma, particularly for large magmatic systems with the potential to produce hazardous eruptions. This has been a persistent open question in volcanology because current estimates based on the end-member compaction and hindered settling models yield timescales that are too slow to explain relatively rapid melt assembly preceding supereruptions (Bachmann & Huber 2019).

Moving beyond two phases, the model is ready to be used to explore three-phase magma dynamics. Before further investigations, however, transport coefficients require more rigorous calibration constrained by experiments and theory. This can be achieved using the Bayesian estimation procedure outlined in this study. With a well-calibrated model for three-phase mixtures containing a magmatic volatile phase (MVP), we can examine the role of the MVP in controlling phase segregation in crustal magmatic systems. Further goals include elucidating how MVP exsolution and migration may pressurize a crustal magma reservoir, either mobilizing melt for eruptions (Degruyter & Huber 2014; Edmonds *et al.* 2019), or releasing fluid pulses into the crust to form porphyry copper and other ore deposits (Chelle-Michou *et al.* 2017). Extensions to three-phase or higher systems containing multiple crystal and melt phases can explore an even wider range of open questions on phase segregation in igneous systems, including ore genesis (e.g. Chung & Mungall 2009; Ovalle *et al.* 2018; Keller *et al.* 2022) and planar-estimal formation (e.g. Elkins-Tanton 2012; Ghanbarzadeh *et al.* 2017; Lichtenberg *et al.* 2019).

## ACKNOWLEDGMENTS

YQW was funded by the European Union's Horizon 2020 research and innovation programme under the Marie Skłodowska-Curie Actions grant agreement number 894897 (project acronym DEFORM). We are grateful to the two reviewers, Harro Schmeling and Samuel Butler, and the editor, Juan Carlos Afonso, for productive discussions that improved the structure and analysis in this manuscript.

## DATA AVAILABILITY

The MATLAB software package to run the multiphase mechanical model is available and regularly updated at <https://github.com/kellertobs/pantarhei.git>. The advection function is included there, but can also be downloaded separately at <https://github.com/yingqiwing/advection.git>. The coefficient calibration routine is at <https://github.com/yingqiwing/pdmcilib.git> and must be accompanied by the parameter estimation toolbox containing CATMIP from <https://github.com/yingqiwing/paramest.git>.

Specific releases of the codes accompanying this paper, as well as scripts to run models and produce the figures can be found at <https://doi.org/10.5281/zenodo.7097590>.

## REFERENCES

- Aharonov, E., Whitehead, J.A., Kelemen, P.B. & Spiegelman, M., 1995. Channeling instability of upwelling melt in the mantle, *J. geophys. Res.*, **100**(B10), 20433–20450.
- Albers, M., 2000. A local mesh refinement multigrid method for 3-D convection problems with strongly variable viscosity, *J. Comput. Phys.*, **160**(1), 126–150.
- Annen, C.J., Blundy, J.D. & Sparks, R.S., 2006. The genesis of intermediate and Silicic magmas in deep crustal hot zones, *J. Petrol.*, **47**(3), 505–539.
- Bachmann, O. & Bergantz, G., 2008. The magma reservoirs that feed supereruptions, *Elements*, **4**(1), 17–21.
- Bachmann, O. & Huber, C., 2016. Silicic magma reservoirs in the Earth's crust, *Am. Mineral.*, **101**(1), 2377–2404.
- Bachmann, O. & Huber, C., 2019. The inner workings of crustal distillation columns; the physical mechanisms and rates controlling phase separation in Silicic magma reservoirs, *J. Petrol.*, **60**(1), 3–18.
- Barcilon, V. & Richter, F.M., 1986. Nonlinear waves in compacting media, *J. Fluid Mech.*, **164**, 429–448.

- Barcilon, V. & Lovera, O.M., 1989. Solitary waves in magma dynamics, *J. Fluid Mech.*, **204**, 121–133.
- Bercovici, D., Ricard, Y. & Schubert, G., 2001. A two-phase model for compaction and damage 1. General theory, *J. geophys. Res.*, **106**(B5), 8887–8906.
- Bergantz, G.W., Schleicher, J.M. & Burgisser, A., 2017. On the kinematics and dynamics of crystal-rich system, *J. geophys. Res.*, **122**(8), 6131–6159.
- Bertolett, E., Prior, D., Gravley, D., Hampton, S. & Kennedy, B., 2019. Compacted cumulates revealed by electron backscatter diffraction analysis of plutonic lithics, *Geology*, **47**(5), 445–448.
- Birnbaum, J., Keller, T., Suckale, J. & Lev, E., 2020. Periodic outgassing as a result of unsteady convection in Ray lava lake, Mount Erebus, Antarctica, *Earth planet. Sci. Lett.*, **530**, doi:10.1016/j.epsl.2019.115903.
- Brandeis, G. & Jaupart, C., 1986. On the interaction between convection and crystallization in cooling magma chambers, *Earth planet. Sci. Lett.*, **77**(3–4), 345–361.
- Caricchi, L. & Blundy, J., 2015. The temporal evolution of chemical and physical properties of magmatic systems, *Geol. Soc., Lond., Spec. Publ.*, **422**(1), 1–15.
- Cashman, K.V. & Giordano, G., 2014. Calderas and magma reservoirs, *J. Volc. Geotherm. Res.*, **288**, 28–45.
- Cashman, K.V. & Edmonds, M., 2019. Mafic glass compositions: a record of magma storage conditions, mixing and ascent, *Phil. Trans. R. Soc., A*, **377**(2139), doi:10.1098/rsta.2018.0004.
- Chelle-Michou, C., Rottier, B., Caricchi, L. & Simpson, G., 2017. Tempo of magma degassing and the genesis of porphyry copper deposits, *Sci. Rep.*, **7**(1), doi:10.1038/srep40566.
- Chung, H.Y. & Mungall, J.E., 2009. Physical constraints on the migration of immiscible fluids through partially molten silicates, with special reference to magmatic sulfide ores, *Earth planet. Sci. Lett.*, **286**(1–2), 14–22.
- Cooper, K.M., 2017. What does a magma reservoir look like? The “crystal’s-eye” view, *Elements*, **13**(1), 23–28.
- Costa, A., Caricchi, L. & Bagdassarov, N., 2009. A model for the rheology of particle-bearing suspensions and partially molten rocks, *Geochem. Geophys. Geosyst.*, **10**(3), 1–13.
- Costa, F., Coogan, L.A. & Chakraborty, S., 2010. The time scales of magma mixing and mingling involving primitive melts and melt-mush interaction at mid-ocean ridges, *Contrib. Mineral. Petrol.*, **159**(3), 371–387.
- Culha, C., Suckale, J., Keller, T. & Qin, Z., 2020. Crystal fractionation by crystal-driven convection, *Geophys. Res. Lett.*, **47**(4), 1–9.
- Degruyter, W. & Huber, C., 2014. A model for eruption frequency of upper crustal Silicic magma chambers, *Earth planet. Sci. Lett.*, **403**, 117–130.
- Dohmen, J. & Schmeling, H., 2021. Magma ascent mechanisms in the transition regime from solitary porosity waves to diapirism, *Solid Earth*, **12**(7), 1549–1561.
- Drew, D.A. & Passman, S.L., 1999. *Theory of Multicomponent Fluids, Vol. 135 of Applied Mathematical Sciences*, Springer New York.
- Driesner, T. & Heinrich, C.A., 2007. The system H<sub>2</sub>O–NaCl. Part I: correlation formulae for phase relations in temperature–pressure–composition space from 0 to 1000°C, 0 to 5000bar, and 0 to 1 XNaCl, *Geochim. Cosmochim. Acta*, **71**(20), 4880–4901.
- Dufek, J. & Bachmann, O., 2010. Quantum magmatism: magmatic compositional gaps generated by melt-crystal dynamics, *Geology*, **38**(8), 687–690.
- Edmonds, M. & Woods, A.W., 2018. Exsolved volatiles in magma reservoirs, *J. Volc. Geotherm. Res.*, **368**, 13–30.
- Edmonds, M., Cashman, K.V., Holness, M. & Jackson, M., 2019. Architecture and dynamics of magma reservoirs, *Phil. Trans. R. Soc., A*, **377**(2139), doi:10.1098/rsta.2018.0298.
- Elkins-Tanton, L.T., 2012. Magma oceans in the inner solar system, *Ann. Rev. Earth planet. Sci.*, **40**(1), 113–139.
- Gerya, T., 2019. *Introduction to Numerical Geodynamic Modelling*, 2nd edn, Cambridge Univ. Press.
- Ghanbarzadeh, S., Hesse, M.A. & Prodanović, M., 2017. Percolative core formation in planetesimals enabled by hysteresis in metal connectivity, *Proc. Natl. Acad. Sci.*, **114**(51), 13406–13411.
- Golabek, G.J., Schmeling, H. & Tackley, P.J., 2008. Earth’s core formation aided by flow channelling instabilities induced by iron diapirs, *Earth planet. Sci. Lett.*, **271**(1–4), 24–33.
- Gutiérrez, F. & Parada, M.A., 2010. Numerical modeling of time-dependent fluid dynamics and differentiation of a shallow basaltic magma chamber, *J. Petrol.*, **51**(3), 731–762.
- Harten, A., 1983. High resolution schemes for hyperbolic conservation laws, *J. Comput. Phys.*, **49**(3), 357–393.
- Hess, H.H., 1960. Stillwater igneous complex, Montana, in *Memoir of the Geological Society of America*, Vol. **80**, pp. 1–240, Geological Society of America.
- Hirth, G. & Kohlstedt, D.L., 1996. Water in the oceanic upper mantle: implications for rheology, melt extraction and the evolution of the lithosphere, *Earth planet. Sci. Lett.*, **144**(1–2), 93–108.
- Hirth, G. & Kohlstedt, D.L., 2003. Rheology of the upper mantle and the mantle wedge: a view from the experimentalists, in *Inside the Subduction Factory*, Vol. **138**, Geophysical Monograph Series, pp. 83–106, ed. Eiler, J., American Geophysical Union.
- Holness, M.B., Vukmanovic, Z. & Mariani, E., 2017. Assessing the role of compaction in the formation of adcumulates: a microstructural perspective, *J. Petrol.*, **58**(4), 643–673.
- Holness, M.B., Stock, M.J. & Geist, D., 2019. Magma chambers versus mush zones: constraining the architecture of sub-volcanic plumbing systems from microstructural analysis of crystalline enclaves, *Phil. Trans. R. Soc., A*, **377**(2139), doi:10.1098/rsta.2018.0006.
- Holtzman, B.K., Groebner, N.J., Zimmerman, M.E., Ginsberg, S.B. & Kohlstedt, D.L., 2003. Stress-driven melt segregation in partially molten rocks, *Geochem. Geophys. Geosyst.*, **4**(5), doi:10.1029/2001gc000258.
- Hoyos, S., Florez, D., Pec, M. & Huber, C., 2022. Crystal shape control on the repacking and jamming of crystal-rich mushes, *Geophys. Res. Lett.*, **49**(19), 1–8.
- Huber, C., Bachmann, O. & Manga, M., 2009. Homogenization processes in Silicic magma chambers by stirring and mushification (latent heat buffering), *Earth planet. Sci. Lett.*, **283**(1), 38–47.
- Huber, C. & Parmigiani, A., 2018. A physical model for three-phase compaction in Silicic magma reservoirs, *J. geophys. Res.*, **123**(4), 2685–2705.
- Jackson, M.D., Blundy, J. & Sparks, R.S., 2018. Chemical differentiation, cold storage and remobilization of magma in the Earth’s crust, *Nature*, **564**(7736), 405–409.
- Jiang, G.-S. & Shu, C.-W., 1996. Efficient implementation of weighted ENO schemes, *J. Comput. Phys.*, **126**(1), 202–228.
- Katz, R.F., Spiegelman, M. & Holtzman, B., 2006. The dynamics of melt and shear localization in partially molten aggregates, *Nature*, **442**(7103), 676–679.
- Katz, R.F., Jones, D. W.R., Rudge, J.F. & Keller, T., 2022. Physics of melt extraction from the mantle: speed and style, *Ann. Rev. Earth planet. Sci.*, **50**(1), doi:10.1146/annurev-earth-032320-083704.
- Katz, R.F., 2008. Magma dynamics with the enthalpy method: benchmark solutions and magmatic focusing at mid-ocean ridges, *J. Petrol.*, **49**(12), 2099–2121.
- Katz, R.F., 2022. *The dynamics of partially molten rock*, Princeton Univ. Press.
- Kelemen, P.B., Whitehead, J.A., Aharonov, E. & Jordahl, K.A., 1995. Experiments on flow focusing in soluble porous media, with applications to melt extraction from the mantle, *J. geophys. Res.*, **100**(B1), 475–496.
- Keller, T., May, D.A. & Kaus, B.J., 2013. Numerical modelling of magma dynamics coupled to tectonic deformation of lithosphere and crust, *J. geophys. Int.*, **195**(3), 1406–1442.
- Keller, T. & Katz, R.F., 2016. The role of volatiles in reactive melt transport in the asthenosphere, *J. Petrol.*, **57**(6), 1073–1108.
- Keller, T. & Suckale, J., 2019. A continuum model of multi-phase reactive transport in igneous systems, *J. geophys. Int.*, **219**(1), 185–222.
- Keller, T., Tornos, F., Hanchar, J.M., Pietruszka, D.K., Soldati, A., Dingwell, D.B. & Suckale, J., 2022. Genetic model of the El Laco magnetite-apatite deposits by extrusion of iron-rich melt, *Nat. Commun.*, **13**(1), 6114, doi:10.1038/s41467-022-33302-z.
- Lapotre, M. G.A., Ehlmann, B.L. & Minson, S.E., 2017. A probabilistic approach to remote compositional analysis of planetary surfaces, *J. geophys. Res.*, **122**(5), 983–1009.
- Leonard, B.P., 1995. Order of accuracy of QUICK and related convection-diffusion schemes, *Appl. Math. Modell.*, **19**(11), 640–653.

- Lichtenberg, T., Keller, T., Katz, R.F., Golabek, G.J. & Gerya, T.V., 2019. Magma ascent in planetesimals: control by grain size, *Earth planet. Sci. Lett.*, **507**, 154–165.
- Lissenberg, C.J., MacLeod, C.J., Howard, K.A. & Godard, M., 2013. Pervasive reactive melt migration through fast-spreading lower oceanic crust (Hess Deep, equatorial Pacific Ocean), *Earth planet. Sci. Lett.*, **361**, 436–447.
- Longo, A., Vassalli, M., Papale, P. & Barsanti, M., 2006. Numerical simulation of convection and mixing in magma chambers replenished with CO<sub>2</sub>-rich magma, *Geophys. Res. Lett.*, **33**(21), doi:10.1029/2006GL027760.
- Lu, T.-Y., He, Z.-Y. & Klemd, R., 2022. Identifying crystal accumulation and melt extraction during formation of high-silica granite, *Geology*, **50**(2), 216–221.
- Manga, M., 1996. Waves of bubbles in basaltic magmas and lavas, *J. geophys. Res.*, **101**(B8), 17 457–17 465.
- Martin, D. & Nokes, R., 1988. Crystal settling in a vigorously convecting magma chamber, *Nature*, **332**(6164), 534–536.
- Mavko, G., Mukerji, T. & Dvorkin, J., 2009. *The Rock Physics Handbook*, Cambridge Univ. Press.
- McKenzie, D., 1984. The generation and compaction of partially molten rock, *J. Petrol.*, **25**(3), 713–765.
- Minson, S.E., Simons, M. & Beck, J.L., 2013. Bayesian inversion for finite fault earthquake source models I-theory and algorithm, *J. geophys. Int.*, **194**(3), 1701–1726.
- Molina, I., Burgisser, A. & Oppenheimer, C., 2012. Numerical simulations of convection in crystal-bearing magmas: a case study of the magmatic system at Erebus, Antarctica, *J. geophys. Res.*, **117**(7), 1–38.
- Mucha, P.J., Tee, S.-Y., Weitz, D.A., Shraiman, B.I. & Brenner, M.P., 2004. A model for velocity fluctuations in sedimentation, *J. Fluid Mech.*, **501**, 71–104.
- Oliveira, B., Afonso, J.C., Zlotnik, S. & Diez, P., 2018. Numerical modelling of multiphase multicomponent reactive transport in the Earth's interior, *J. geophys. Int.*, **212**(1), 345–388.
- Ovalle, J.T. et al., 2018. Formation of massive iron deposits linked to explosive volcanic eruptions, *Sci. Rep.*, **8**(1), 1–11.
- Philpotts, A.R. & Philpotts, D.E., 2005. Crystal-mush compaction in the Cohasset flood-basalt flow, Hanford, Washington, *J. Volc. Geotherm. Res.*, **145**(3–4), 192–206.
- Pietrzak, J., 1998. The use of TVD limiters for forward-in-time upstream-biased advection schemes in ocean modeling, *Mon. Wea. Rev.*, **126**(3), 812–830.
- Polyak, B., 1964. Some methods of speeding up the convergence of iteration methods, *USSR Comput. Math. Math. Phys.*, **4**(5), 1–17.
- Qin, Z. & Suckale, J., 2017. Direct numerical simulations of gas-solid-liquid interactions in dilute fluids, *Int. J. Multiphase Flow*, **96**, 34–47.
- Rabinowicz, M., Genthon, P., Ceuleneer, G. & Hillairet, M., 2001. Compaction in a mantle mush with high melt concentrations and the generation of magma chambers, *Earth planet. Sci. Lett.*, **188**(3–4), 313–328.
- Räss, L., Duretz, T. & Podladchikov, Y., 2019. Resolving hydromechanical coupling in two and three dimensions: spontaneous channelling of porous fluids owing to decompaction weakening, *J. geophys. Int.*, **218**(3), 1591–1616.
- Räss, L., Utkin, I., Duretz, T., Omlin, S. & Podladchikov, Y.Y., 2022. Assessing the robustness and scalability of the accelerated pseudo-transient method, *Geosci. Model Dev.*, **15**(14), 5757–5786.
- Rees Jones, D.W., Katz, R.F., Tian, M. & Rudge, J.F., 2018. Thermal impact of magmatism in subduction zones, *Earth planet. Sci. Lett.*, **481**, 73–79.
- Richard, G.C., Kanjilal, S. & Schmeling, H., 2012. Solitary-waves in geophysical two-phase viscous media: a semi-analytical solution, *Phys. Earth planet. Inter.*, **198–199**, 61–66.
- Richardson, J. & Zaki, W., 1954. The sedimentation of a suspension of uniform spheres under conditions of viscous flow, *Chem. Eng. Sci.*, **3**(2), 65–73.
- Roscoe, R., 1952. The viscosity of suspensions of rigid spheres, *Br. J. Appl. Phys.*, **3**(8), 267–269.
- Rudge, J.F., Bercovici, D. & Spiegelman, M., 2011. Disequilibrium melting of a two phase multicomponent mantle, *J. geophys. Int.*, **184**(2), 699–718.
- Rudge, J.F., 2018. The viscosities of partially molten materials undergoing diffusion creep, *J. geophys. Res.*, **123**(12), 534–10.
- Ruprecht, P., Bergantz, G.W. & Dufek, J., 2008. Modeling of gas-driven magmatic overturn: tracking of phenocryst dispersal and gathering during magma mixing, *Geochem. Geophys. Geosyst.*, **9**(7), doi:10.1029/2008GC002022.
- Salari, K. & Knupp, P., 2000. Code Verification by the Method of Manufactured Solutions, Tech. rep., Sandia National Laboratories (SNL), Albuquerque, NM, and Livermore, CA.
- Schmeling, H., Marquart, G., Weinberg, R. & Wallner, H., 2019. Modelling melting and melt segregation by two-phase flow: new insights into the dynamics of magmatic systems in the continental crust, *J. geophys. Int.*, **217**(1), 422–450.
- Scott, D.R. & Stevenson, D.J., 1984. Magma solitons, *Geophys. Res. Lett.*, **11**(11), 1161–1164.
- Scott, D.R. & Stevenson, D.J., 1986. Magma ascent by porous flow, *J. geophys. Res.*, **91**(B9), doi:10.1029/JB091iB09p09283.
- Segrè, P.N., Liu, F., Umbanhowar, P. & Weitz, D.A., 2001. An effective gravitational temperature for sedimentation, *Nature*, **409**(6820), 594–597.
- Simpson, G., Spiegelman, M. & Weinstein, M.I., 2010. A multiscale model of partial melts: I. Effective equations, *J. geophys. Res.*, **115**(B4), doi:10.1029/2009JB006375.
- Simpson, G. & Spiegelman, M., 2011. Solitary wave benchmarks in magma dynamics, *J. Sci. Comp.*, **49**(3), 268–290.
- Snyder, D., 2000. Thermal effects of the intrusion of basaltic magma into a more Silicic magma chamber and implications for eruption triggering, *Earth planet. Sci. Lett.*, **175**(3–4), 257–273.
- Sparks, R. S.J., Huppert, H.E., Turner, J.S., Sakuyama, M. & O'Hara, M.J., 1984. The fluid dynamics of evolving magma chambers, *Phil. Trans. R. Soc. Lond., A*, **310**(1514), 511–534.
- Sparks, R. S.J., Annen, C., Blundy, J.D., Cashman, K.V., Rust, A.C. & Jackson, M.D., 2019. Formation and dynamics of magma reservoirs, *Phil. Trans. R. Soc. Lond., A*, **377**(2139), doi:10.1098/rsta.2018.0019.
- Spiegelman, M., Kelemen, P.B. & Aharonov, E., 2001. Causes and consequences of flow organization during melt transport: The reaction infiltration instability in compactible media, *J. geophys. Res.*, **106**(B2), 2061–2077.
- Spiegelman, M., 1993a. Flow in deformable porous media. Part 1: simple analysis, *J. Fluid Mech.*, **247**, 17–38.
- Spiegelman, M., 1993b. Flow in deformable porous media. Part 2: numerical analysis – the relationship between shock waves and solitary waves, *J. Fluid Mech.*, **247**, 39–63.
- Stevenson, D.J. & Scott, D.R., 1991. Mechanics of fluid-rock systems, *Ann. Rev. Fluid Mech.*, **23**(1), 305–339.
- Stevenson, D.J., 1989. Spontaneous small-scale melt segregation in partial melts undergoing deformation, *Geophys. Res. Lett.*, **16**(9), 1067–1070.
- Sweby, P.K., 1984. High resolution schemes using flux limiters for hyperbolic conservation laws, *SIAM J. Numer. Anal.*, **21**(5), 995–1011.
- Trompert, R.A. & Hansen, U., 1996. The application of a finite volume multigrid method to three-dimensional flow problems in a highly viscous fluid with a variable viscosity, *Geophys. Astrophys. Fluid Dyn.*, **83**(3–4), 261–291.
- Wang, L.H., Yarushina, V.M., Alkhimenkov, Y. & Podladchikov, Y., 2021. Physics-inspired pseudo-transient method and its application in modelling focused fluid flow with geological complexity, *J. geophys. Int.*, **229**(1), 1–20.
- Weatherley, S.M. & Katz, R.F., 2012. Melting and channelized magmatic flow in chemically heterogeneous, upwelling mantle, *Geochem. Geophys. Geosyst.*, **13**(5), doi:10.1029/2011GC003989.
- Wiggins, C. & Spiegelman, M., 1995. Magma migration and magmatic solitary waves in 3-D, *Geophys. Res. Lett.*, **22**(10), 1289–1292.
- Wong, Y. & Segall, P., 2019. Numerical analysis of time-dependent conduit magma flow in dome-forming eruptions with application to Mount St. Helens 2004–2008, *J. geophys. Res.*, **124**(11), 11 251–11 273.
- Zahn, K., Méndez-Alcaraz, J.M. & Maret, G., 1997. Hydrodynamic interactions may enhance the self-diffusion of colloidal particles, *Phys. Rev. Lett.*, **79**(1), 175–178.

Zieg, M.J. & Marsh, B.D., 2012. Multiple reinjections and crystal-mush compaction in the Beacon Sill, McMurdo Dry Valleys, Antarctica, *J. Petrol.*, **53**(12), 2567–2591.

Šrámek, O., Ricard, Y. & Dubuffet, F., 2010. A multiphase model of core formation, *J. geophys. Int.*, **181**(1), 198–220.

## SUPPORTING INFORMATION

Supplementary data are available at [GJI](#) online.

### suppl\_data

Please note: Oxford University Press is not responsible for the content or functionality of any supporting materials supplied by the

authors. Any queries (other than missing material) should be directed to the corresponding author for the paper.

## APPENDIX A: ADVECTION SCHEME

In the volume transfer  $\Gamma_{\phi}^i$ , phase fraction is advected with the reference velocity field,  $\mathbf{v}^* \cdot \nabla \phi^i$  (2a). Calculating advection using central differencing, as is done for the flux divergence terms, can produce oscillations that intensify with simulation time step. One could avoid this numerical dispersion by applying the first order

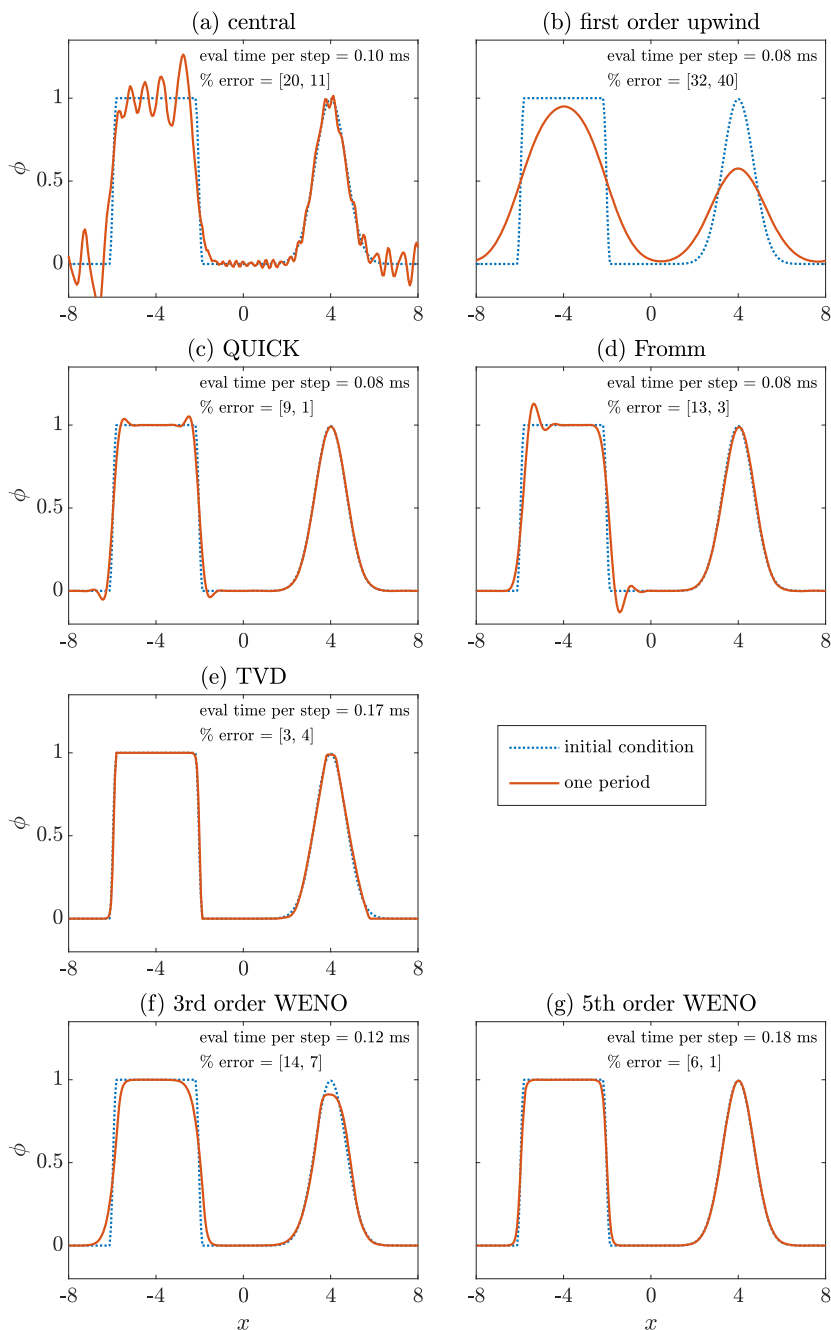


**Figure A1.** Test of the seven advection schemes on a 1-D toy problem with a square wave and a Gaussian, which move to the right with a non-dimensional velocity of 1. There are 256 points in the  $x$  direction. Each panel shows the initial condition (blue) and the solution after one domain traverse of the wave (red), along with the time taken (in milliseconds) to evaluate one time step and the 2-norm percent error for the [square wave, Gaussian] parts of the perturbation.



upwind scheme, however this produces strong numerical diffusion and compromises the overall accuracy of the numerical scheme.

To calculate the advection of phase fraction more accurately, we have integrated a general function into the numerical model that contains seven options for advection on a staggered grid: (i) central averaging and (ii) first order upwind as baselines, (iii) the Quadratic Upstream Interpolation for Convective Kinematics (QUICK) scheme (Leonard 1995), (iv) the Fromm scheme (Trompert & Hansen 1996), (v) the Total Variation Diminishing (TVD) scheme using the ‘Superbee limiter’ (Harten 1983; Sweby 1984; Pietrzak 1998) and the (vi) third and (vii) fifth order Weighted Essentially Non-Oscillatory (WENO) schemes (Jiang & Shu 1996). The TVD scheme is a shock-preserving scheme that minimizes oscillations by introducing an additional flux, obtained through the difference between a higher order and lower order flux (‘limited’) approximation. WENO schemes approximate the advected quantity on cell faces using a weighted sum of polynomials constructed using different stencils. The weights are determined by the smoothness of each polynomial, where smoother options are preferred, therefore minimizing oscillations in the advected quantity. All schemes apply a flux-conservative approach: the schemes approximate the advected quantity (in this case phase fraction) on the cell face, which is then combined with the velocities that are already defined there in the staggered grid discretization. All schemes can be employed with closed, open, fixed or periodic boundary conditions. The advection function and demo scripts can be downloaded from the link in the Data Availability statement.

We demonstrate the performance of each advection scheme using a 1-D toy problem where a square wave and a Gaussian are transported to the right in a periodic domain with a constant, non-dimensional velocity of 1. There are 256 gridpoints. We advance the problem in time using the fourth-order Runge–Kutta method. The expected numerical dispersion and diffusion emerge from the central and first order upwind schemes respectively, giving large errors (Figs A1a and b). The QUICK and Fromm schemes generally reproduce the solution well with only minor oscillations at the edges of the square wave (Figs A1c and d). The higher complexity schemes — TVD, WENO (Figs A1e, f and g) — do not exhibit oscillations, although the third order WENO displays marked numerical diffusion on both perturbations.

Multiphase magma transport models have demonstrated good performance of the QUICK (e.g. Wong & Segall 2019), Fromm (e.g. Albers 2000; Katz 2008), TVD (e.g. Šrámek *et al.* 2010) and fifth order WENO schemes (e.g. Qin & Suckale 2017). Based on the above analysis, either QUICK or the fifth order WENO schemes are good choices for the multiphase model in this study. In cases where the phase fraction gradients are generally small and smooth like the Gaussian, one could apply the more efficient QUICK scheme because it preserves the magnitude of the advected quantity well. Furthermore, any oscillations that arise remain small. When sharp boundaries emerge, the fifth order WENO scheme is a better choice because it reproduces sharp gradients well and avoids numerical dispersion prominent from the central differencing scheme (Fig. A2

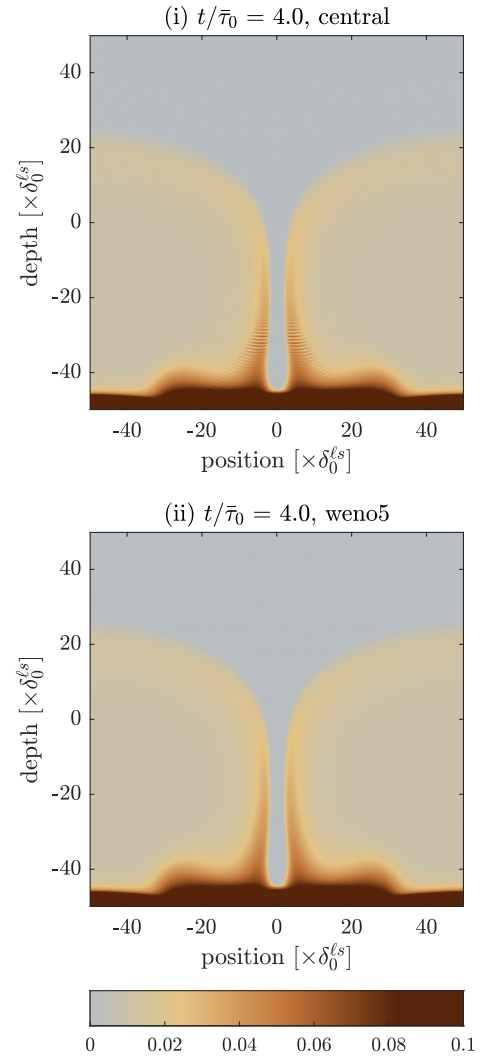


**Figure A2.** Impact of the choice of advection scheme on the 2-D mixture convection simulations for the numerical model presented in this study. Panel (i) uses the central differencing scheme and exhibits numerical dispersion that grows in time, while (ii) uses the fifth order WENO scheme and avoids such dispersion. As a result, the fifth order WENO simulation can also be run to longer time.

and Video S5). The higher computational cost of the fifth order WENO does not severely prolong evaluation time because advection is only calculated when phase fractions are updated every `nupd` iterations in the pseudo-transient solver. Although the TVD scheme has the lowest error for the square wave, we do not choose it because smooth gradients appear to be artificially steepened as shown by the higher error on the Gaussian perturbation, thus TVD is more suitable for problems with strong shocks.

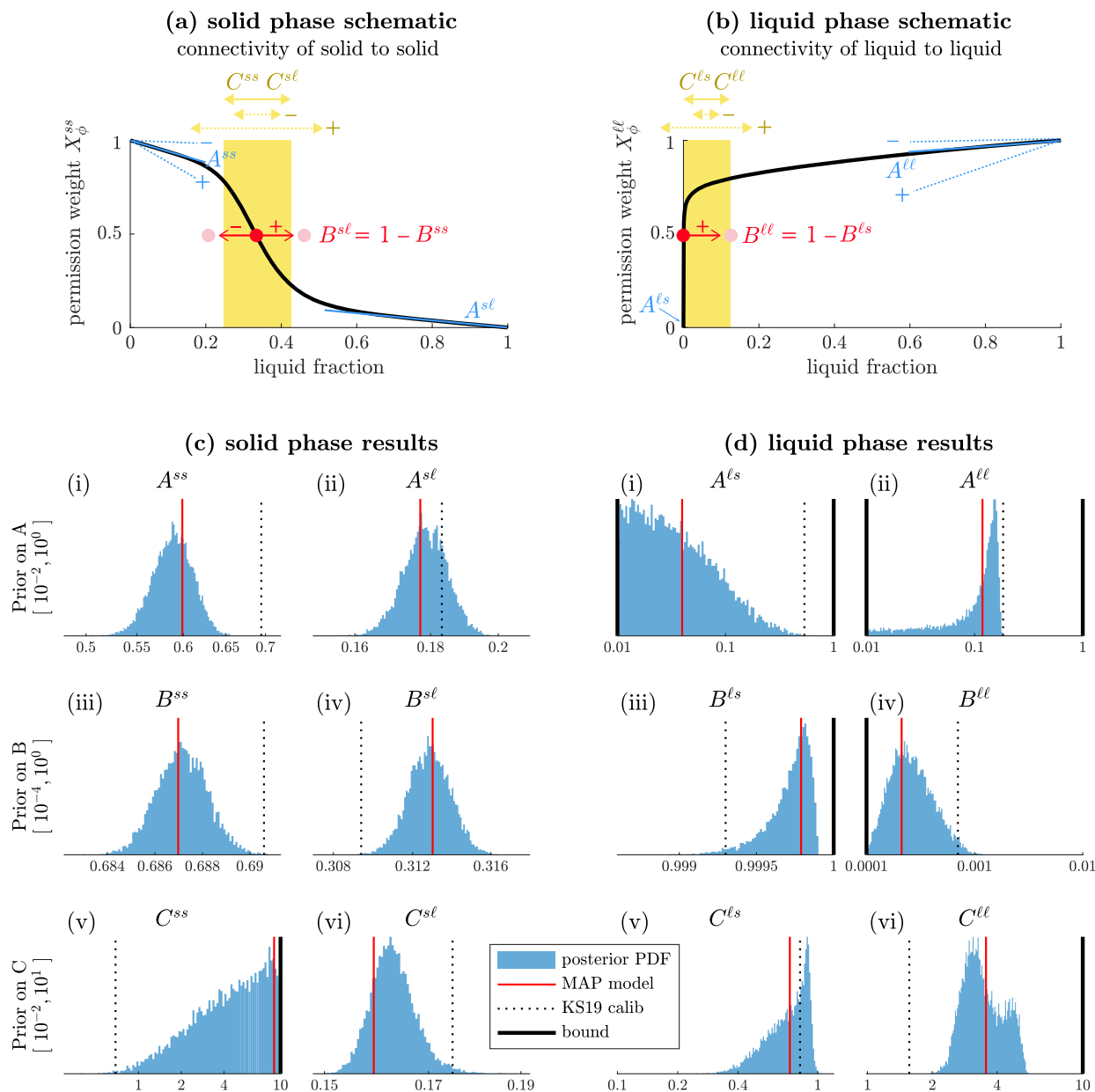


**Figure A3.** Calibration of the fitting parameters  $A$ ,  $B$ ,  $C$  in the permission functions using CATMIP for each phase. Top row shows schematics describing the effect of increasing (+) or decreasing (−) each parameter for the (a) solid phase and (b) liquid phase. Posterior distributions for the (c) solid phase and (d) liquid phase, where the red vertical line marks the maximum *a posteriori* (MAP) model, while the black dotted line marks the model from the previous calibration of Keller & Suckale (2019). Thick black lines mark the prior bounds if they are near the posterior distributions. The priors for each parameter are listed in the left.

## APPENDIX B: CALIBRATION OF PERMISSION WEIGHT PARAMETERS USING CATMIP

We calibrate the parameters  $A$ ,  $B$ ,  $C$  of the permission functions using the Cascading Adaptive Transitional Metropolis in Parallel (CATMIP), a Bayesian inversion algorithm (Minson *et al.* 2013). Each fitting parameter contains  $n \times n$  elements for an  $n$ -phase mixture. For the two-phase mixture in this study, this gives a total of 12 parameters. The parameters describe a smooth step function:  $A$  controls the slope of the permission weights in the pure-phase limits of the phase space,  $B$  controls the critical phase fraction of the step

change, while  $C$  controls the step width (Fig. A3, schematics in panels a, b).

Bayes' Theorem states that the posterior probability of the  $k$ th set of fitting parameters  $P(A_k, B_k, C_k | \mathcal{E})$  is given by

$$P(A_k, B_k, C_k | \mathcal{E}) \propto P(\mathcal{E} | A_k, B_k, C_k) P(A_k, B_k, C_k), \quad (\text{B1})$$

where  $\mathcal{E}$  represents the experimental and theoretical constraints as described in Section 4.  $P(\mathcal{E} | A_k, B_k, C_k)$  is the likelihood which describes how well the  $k$ th parameter set fits the constraints, while  $P(A_k, B_k, C_k)$  is the prior probability. We choose this Bayesian approach because it naturally encodes prior information. While

the two-phase example in this study has ample experimental and theoretical constraints, other mixtures, particularly those with a larger number of phases, may not. Through the prior distribution, the Bayesian approach offers a way to naturally incorporate conceptual information.

To apply this Bayesian approach, we need to define the likelihood and prior probability. For the likelihood, we use a Gaussian error model with a standard deviation of  $0.5 \log_{10}$  units to prefer models within one order of magnitude of the constraints. Using a wider standard deviation should simply return wider posterior distributions as more models would fit the constraints. For the prior, we assume a wide, uniform distribution in  $\log_{10}$  space, which performs better than priors in linear space for problems with non-negative parameters. Prior bounds for elements in  $A$  are set as  $[10^{-2}, 1]$ , for  $B$   $[10^{-4}, 1]$  and for  $C$   $[10^{-2}, 10]$ . Although elements of  $B$  for each phase should sum to 1 and thus correspond to  $n - 1$  free parameters per phase, here we define them independently and then normalize the combination. While this approach results in highly correlated posterior distributions for the elements of  $B$ , our tests found that this choice performs better by avoiding extremely low acceptance rates, when compared to tests imposing ‘sum to unity’ conditions in the prior calculation. Future calibrations may test the application of the Dirichlet distribution which ensures that the elements of  $B$  sum to unity (Lapotre *et al.* 2017).

Using the CATMIP calibration, the posterior probability distribution generally show narrowed constraints relative to the prior (Fig. A3). Where the posterior distributions are near the prior bounds, we mark the prior bounds with thick black lines. The *maximum a posteriori* (MAP) model is marked by the red line, while parameters from the previous calibration from Keller & Suckale (2019) are shown by the black dotted line.

For the solid phase,  $A^{ss}$ ,  $A^{sl}$ ,  $B^{ss}$ ,  $B^{sl}$ ,  $C^{sl}$  show posterior distributions that are much narrower than the imposed priors, as indicated

by the narrow range of values and the absence of a black prior bound in their plots (panels i–iv and vi of Fig. A3c). The MAP model lies close to the mode of the distributions. Although the model from the previous calibration (black dotted lines) does not always lie within the posterior distribution, they are actually very close considering the narrow range of values relative to the width of the prior. In contrast,  $C^{ss}$  [Fig. A3 c(v)] is less well-constrained by the inversion, as the posterior distribution occupies a wide range and pushes against the upper bound. We note, however, that varying  $C^{ss}$  between the previous value of 0.6889 to the new MAP value of 9.0105 actually shows minimal impact on the shape of the permission weight.

For the liquid phase, the slope of the connectivity of the liquid to the solid  $A^{ls}$  is poorly constrained, as shown by the wide space it occupies within the prior, while  $A^{ll}$  shows improved constraints with preferred values around 0.1 (panels i, ii of Fig. A3d). This result can be understood in the context of  $B^{ls}$ ,  $B^{ll}$  (panels iii, iv of Fig. A3d): the value of  $B^{ls}$  close to 1, complemented by the small value of  $B^{ll}$ , reflects the high degree of connectivity of the liquid at low liquid fractions. Therefore  $A^{ls}$ , which determines the slope of the permission weight below the percolation threshold, occupies a miniscule part of the phase space and thus cannot be well-constrained in the inversion. This result is consistent with the previous calibration (black dotted lines), but yield slightly more extreme values on  $B$ , which we interpret to be the effect of performing the calibration in  $\log_{10}$  instead of linear space. The step widths  $C^{ls}$ ,  $C^{ll}$  show improved constraints relative to the prior (panels v, vi of Fig. A3d). Notably, we also discover a strong negative correlation between  $A^{ll}$  and both  $C$  parameters, reflecting their non-uniqueness in determining the shape of the liquid–liquid connectivity curves (Fig. S7). Increasing the slope of the liquid–liquid connectivity is complemented by a narrower step width. This negative correlation explains the difference between the MAP model and the previous calibration for the value of  $C^{ll}$ .